Fatty Acid Metabolism and The Oxidative Stress Response Support Bacterial Predation

Rikesh Jain*(1), Nguyen-Hung Le*(1), Lionel Bertaux(2), Jean Baudry(3), Jérôme Bibette(3), Yann Denis(4), Bianca H. Habermann(5), Tâm Mignot#(1)

* Equal Contribution

Correspondence: tmignot@imm.cnrs.fr

Affiliation:

(1) Aix-Marseille Université - CNRS UMR 7283, Institut de Microbiologie de la Méditerranée and Turing Center for Living Systems, Marseille, France

(2) Aix-Marseille Université - CNRS UMR 7283, Institut de Microbiologie de la Méditerranée, Marseille, France

(3) Laboratoire Colloïdes et Matériaux Divisés, Institut Chimie, Biologie, Innovation, UMR 8231, ESPCI Paris, CNRS, Université Paris Sciences et Lettres, 75005 Paris, France

(4) Aix-Marseille Université – CNRS FR3479, Institut de Microbiologie de la Méditerranée, Marseille, France

(5) Aix Marseille University, CNRS, IBDM UMR 7288, Turing Center for Living Systems, Marseille, France

Abstract

Despite growing awareness for their importance in soil ecology, the genetic and physiological traits of bacterial predators are still relatively poorly understood. In the course of a *Myxococcus xanthus* predator evolution experiment, we discovered a class of genotypes leading to enhanced predation against evolutionary-diverse species. Genetics and RNAseq analyses link this improved predation capacity to the fine-tuned control of intracellular Acetyl-CoA pools following increased activation of fatty acid beta-oxidation. Notably, these metabolic changes led to the constitutive expression of antioxidant genes. This is critical to the predatory advantage of the evolved strain because this response shields predatory cells against Reactive Oxygen Species (ROS), which arise following contact-dependent killing of the prey cells. Globally, these findings suggest that predators turning on lipid metabolism serves two purposes: energy production and adaptation to oxidative stress originating from interaction with their prey.

Significance Statement

This study sheds light on the underexplored genetic and metabolic strategies employed by bacterial predators within soil ecosystems. Through experimental evolution in *Myxococcus xanthus*, we have observed that more efficient predators tend to accumulate mutations that modify the intracellular Acetyl-CoA flux, leading to a metabolic shift favoring fatty acid degradation for energy production. One significant outcome of this adaptation is the constant expression of antioxidant genes, aimed at mitigating oxidative stress and providing heightened protection against reactive oxygen species generated during prey cell lysis. This adaptive mechanism proves advantageous across a diverse range of prey species, highlighting a potential role of metabolic adaptation in the evolutionary trajectory of bacterial predators within their authentic ecological niche.

Introduction

Intensive agriculture and the systematic use of chemicals over decades of practice has deprived soil microbial biodiversity, greatly endangering food chain productivity in a relatively short term(1, 2). Restoring these ecosystems could pave the way to more sustainable practices, which is especially urgent given that this problem is aggravated by global warming(3). Bacterial predators have recently come to the forefront for their role in shaping microbial soil ecosystems (4, 5). Among them, the *Myxobacteria* act potentially as key taxa within the microbial food web(4, 6, 7). Characterized as generalist predators, *Myxobacteria* feed on a vast array of microorganisms, including diverse bacterial and fungal species(8). Their predatory nature offers promising avenues in combating plant infections. Notably, certain species of *Myxobacteria* have shown to efficiently counteract infections from various pests, spanning from fungi to pathogenic bacteria(9, 10). Therefore, understanding how these predators interact with their preys and digest them could help determine and leverage their function in soil ecology.

Predation in *Myxobacteria* is a complex interplay of various factors, from motility and secretion of secondary metabolites to specialized mechanisms of contact-dependent killing. We and others recently discovered that when *Myxococcus xanthus* cells establish contact with the prey cells, they temporarily halt motility and activate two unique cellular machineries – a suspected Tad pilus-like system (Kil) and an unconventional Type-3 secretion system (T3SS)(11, 12). These systems act sequentially to trigger prey cell plasmolysis (Kil), and subsequently lyse the dead prey cells (T3SS) to obtain the nutrients that fuel *Myxococcus* growth(12). On the chromosome, the *kil* and *t3ss* systems are encoded by three prominent genetic clusters, collectively comprising over 60 anticipated genes(12–14). This large genetic repertoire is likely associated with the high versatility of the Kil/T3SS system, which can detect and kill a diverse array of monoderm and diderm bacterial species of distinct evolutionary origins and ecologies (action against fungi has not been tested(15, 16)).

Contact-dependent killing is only the first step of the process. Downstream, several metabolic adaptations also participate in the predation process. *Myxococcus* must also metabolize prey-derived nutrients and overcome potential prey defenses. This was suggested by transcriptomic studies encompassing diverse prey species, which consistently unveiled substantial shifts in the genetic expression profiles (17–19). In addition to the *kil* genes, lytic enzymes and genes encoding secondary metabolites, metabolic genes encoding iron siderophore pathways and fatty acid degradation are systematically induced(14, 17, 18).

To explore the physiological changes that occur during predation and what genetic pathways are required during such an atypical growth phase, we conducted experimental evolution selecting for enhanced predation by the *Myxococcus* DZ2 laboratory strain. The rationale was that by identifying the traits that evolve to improve predation, we may gain insight into unknown mechanisms of predation and predator-prey interactions. Our data suggest that predation involves a profound metabolic shift towards fatty acid consumption and adaptation to an elevated accumulation of reactive oxygen species (ROS) originating from distinct prey- and predator-dependent mechanisms.

Results

Conserved *Myxococcus* transcriptional response across different prey

To determine if there is a core genetic response to predation, we sequenced the *Myxococcus* transcriptome during interactions with three different prey species—*Escherichia coli*, *Bacillus subtilis*, and *Caulobacter crescentus*—under uniform experimental conditions (see Methods).

Echoing previous findings(17, 18), *Myxococcus* demonstrated significant changes in gene expression (wald test, $p.adj < 0.05$) in response to each prey: 2165 genes with *E. coli*, 2379 genes with *B. subtilis*, and 3575 genes with *C. crescentus* (Figure 1A-1C, SI Table1). While overall gene expression profiles showed parallels between interactions with *E. coli* and *B. subtilis*, they differed markedly when *Myxococcus* encountered *C. crescentus* (Figure S1). The underlying mechanisms for this disparity warrant further investigation.

We subsequently focused on gene responses that were consistent across all three prey species (Figure 1D). 1338 *M. xanthus* genes (SI Table2) exhibited differential expression upon *M. xanthus* encounters with any prey. Remarkably, out of these 1338 genes, a staggering 1329 (>99%) showed a consistent pattern, whether it being upregulation or downregulation, across all three comparisons. To gain further insights, we conducted Gene Ontology (GO) analysis based on the current *Myxococcus* genome annotation, with a focus on enrichment in two domains: Biological Processes (BP) and Molecular Function (MF). GO analysis revealed enrichment of the functions tied to translation, respiration, metabolism, and amino acid biosynthesis (in particular Glutamine), suggesting that *Myxococcus* undergoes active growth when exposed to these prey species (See Figures 1E and 1F). In line with previous studies, we also observed an enrichment of genes associated with secondary metabolite production and degradative enzymes, such as proteases and peptidases (Figures 1E and 1F). Intriguingly, both regulatory and chemotaxis systems, especially the Ser/Thr kinases, exhibited changes (Figures 1E and 1F). While the biological functionality of the majority of *M. xanthus* Ser/Thr kinase systems (encompassing over 100 modules) remain unclear(20), it is possible that many are predominantly operational during the predation phase. Lastly, we noted that genes linked to the oxidative stress response were ubiquitously enriched across all three interactions.

Enhanced predatory capabilities of *Myxococcus* variant on *E. coli* prey

RNAseq provided insights into physiological patterns related to predation. To identify which of these adaptations are crucial, we next aimed to identify gain-of-function variants that exhibit improved predatory efficiency.

To this end, we employed *E. coli* as prey. Plating a *Myxococcus* colony adjacent to an *E. coli* colony on a CF medium (detailed in Methods) results in total predation of the prey within 72 hours (Figure 2A). However, when the medium is supplemented by glucose, a sugar that *E. coli* can consume but not *Myxococcus*(21), prey growth is observed and predation is not as efficient (Figure 2A). In fact, predation is completely inhibited at glucose concentrations exceeding 0.1%. This property allowed for an evolution experiment to select superior predatory phenotypes by increasing the concentration of glucose in the media, thereby enhancing prey resistance through evolutionary cycles (Figure 2B). We thus inoculated *Myxococcus* at the center of an *E. coli* colony and allowed a full predatory cycle before transferring to a fresh *E. coli* plate for a new cycle, gradually increasing glucose concentration every 5 cycles (Figure 2B). After 20 cycles and approximately 600 generations of *M. xanthus* (approx. 5 months), we isolated one clone (M1) capable of killing *E. coli* at 0.1% glucose concentration (Figure S2). Glucose uptake in *E. coli* results in acetate release and consequently, medium acidification.

127 Considering that *Myxococcus* can adapt to acid stress via the secretion of diffusible
128 molecules(22), we ascertained that the M1 phenotype was not a consequence of such
129 adaptation, confirming the superior performance of the M1 over the WT in a buffered milieu
130 (Figure S3).

131 To rule out any effect that would be linked to glucose adaptation rather than changes in
132 predatory traits, we compared the killing capacity of the M1 and WT strains at a glucose
133 concentration that is permissive for WT predation (0.075%). Counting *E. coli* colony-forming
134 units post 24 hours of co-incubation with *Myxococcus* (see Methods), revealed that while the
135 WT only killed ~90% of the prey colony, the M1 strain eradicated it entirely (Figure 2C).
136 Investigating whether the elevated predatory efficiency of the M1 correlates with growth and
137 fitness enhancement, we directly quantified *Myxococcus* growth on *E. coli* prey using
138 quantitative digital PCR (see Methods). For the first 24 hours, the WT and M1 variants
139 displayed equivalent growth, but M1 peaked at a higher level by 48 hours, implying a
140 physiological fitness advantage (Figure 2D). As expected, a Δ*kil* mutant did not grow in these
141 conditions, confirming that this assay scores prey-dependent *Myxococcus* growth. We conclude
142 that the M1 variant has evolved enhanced predatory capacities over its WT ancestor, which we
143 further investigated.

144 We subsequently assessed whether the enhanced predatory capacity against *E. coli* was a
145 specific adaptation or a more general evolved trait effective against other bacterial preys, *B.*
146 *subtilis* and *C. crescentus*. The predation efficiency was enhanced against both prey species,
147 although to a lesser extent against *C. crescentus* (Figures 2E and 2F). Thus, the M1 strain
148 contains a selected trait(s) that boosts *Myxococcus* ability to target various prey species.

149 **Genetic basis of superior predatory phenotypes**

150 We next set out to identify the genetic mutations underlying the M1 phenotype. As previously
151 noted, the M1 strain was derived after 20 serial passages (~600 generations) in our evolution
152 experiment. In fact, the M1 phenotype emerged from a progenitor clone (C10E9) displaying an
153 intermediate enhanced predatory phenotype (Figure 3A and 3B). This suggested that the C10E9
154 clone represents an evolutionary intermediate on the path to the emergence of the M1 strain.

155 We sequenced the genomes of both the C10E9 and M1 strains. The C10E9 clone bore three
156 single nucleotide polymorphisms (SNPs): one leading to a D76N alteration in a histidine kinase
157 protein (MXAN_7439) located upstream of the EspI response regulator implicated in
158 Exopolysaccharide (ESP) synthesis(23), and two in a gene hypothesized to encode an Acetate-
159 CoA ligase (MXAN_5856). The impact of the D76N mutation in MXAN_7439 remains
160 ambiguous (Figure S4). Conversely, the premature stop codon mutation (W396*) in Acetate-
161 CoA ligase MXAN_5856 results in the truncation of its C-terminal domain, encompassing
162 residues 531-609 (Figure S5). This domain is analogous to the C-terminal region in *Salmonella*
163 *enterica* Acetate-CoA ligase AcsA (Figure S5)(24). Given the critical role of this domain in
164 Acetyl-CoA synthesis, the W396* mutation likely leads to enzymatic inactivation in the C10E9
165 clone(24). M1 genome sequencing revealed two supplementary SNPs: one in a gene putatively
166 encoding a cytochrome c peroxidase (CytC, MXAN_5562) and another in a gene for a putative
167 Acyl-CoA Thioesterase (ACOT, MXAN_2590, Figure 3A). These mutations each resulted in
168 amino acid changes: a S114L substitution in the cytochrome c peroxidase protein and an M61I
169 substitution in the ACOT protein.

170 Our analysis indicates a two-step evolution of the M1 phenotype: initial mutations gave rise to
171 the C10E9 phenotype, which was subsequently bolstered, potentially by up to two additional
172 mutations. To establish the significance of the CytC or ACOT mutations for the M1 phenotype,
173 we introduced these changes into the WT strain and restored the WT sequences into the M1

174 strain using allelic exchange. The changes in CytC sequence (L114S in M1or S114L in WT)
175 did not change the predatory capabilities of either strain, indicating that the CytC mutation is
176 not critical for the M1 phenotype (Figure 3C). In contrast, introducing the ACOT M61I
177 substitution in the WT background significantly improved its predatory performance, albeit not
178 to M1 level (Figure 3C). Conversely, reintroducing the WT I61M ACOT allele into M1 nearly
179 nullified its predatory edge (Figure 3C). Thus, the M61I mutation in ACOT largely defines the
180 M1 phenotype. Curiously, reverting the ACOT sequence to its WT form does not convert the
181 predatory capability of the M1 to the C10E9 level. This indicates that the CytC mutation likely
182 influenced the evolution of the M1 (see discussion). Finally, an in-frame deletion of the *acot*
183 gene in both WT and M1 strains drastically impaired predation (Figure 3D), underscoring an
184 important role for ACOT in *Myxococcus* predation and demonstrating that the M61I mutation
185 is a gain-of-function alteration.

186 **Evolved predator strains express a predatory metabolic program constitutively**

187 The evolution of the M1 strain appears linked to mutations that map to genes encoding enzymes
188 linked to Acetyl-CoA, a predicted Acetyl-CoA Ligase and a predicted Acyl-CoA Thioesterase
189 ACOT. Acetate Ligase catalyzes the conversion of Acetate and CoA precursors into Acetyl-
190 CoA(24). Remarkably, Acyl-CoA thioesterase performs the opposite reaction and liberates
191 Acetate and CoA(25). These are predicted functions but they suggest that metabolic changes
192 linked to Acetyl-CoA are at the core of the M1 phenotype. Acetyl-CoA is at the crossroad of
193 catabolic and anabolic pathways and can be obtained from both Acetate and fatty acids β-
194 oxidation to fuel the TCA cycle and ATP synthesis through oxidative phosphorylation, and it
195 can serve as precursor for fatty acids biosynthesis (Figure 4A). We therefore screened the
196 *Myxococcus* genomes for genes annotated to encode enzymes in each of these metabolic
197 modules (SI Table3) and compared their transcription patterns in the WT and evolved strains
198 by RNAseq.

199 We found that WT cells induce the expression of fatty acids β-oxidation pathway genes in the
200 presence of all three preys, indicating that FA metabolism is a prey-dependent response,
201 consistent with other reports (Figure S6A,(17, 18)). Remarkably, this response is highly
202 upregulated in both the C10E9 and M1 strain as compared to the WT in absence of prey (Figure
203 4B, Figure S6), suggesting that these variants express a predatory metabolic program
204 constitutively. To further test how the global predator physiology was impacted across the
205 evolutionary path to the M1 phenotype, we assessed the constitutive expression patterns of
206 genes involved in the TCA cycle and Electron Transport Chain (Figure 4C and 4D). Genes
207 related to TCA were upregulated in the C10E9 strain but not in the M1 strain (Figure 4C).
208 Remarkably, the ETC genes were downregulated in both evolved strains as compared to the
209 WT (Figure 4D)

210 Collectively, these results suggest that the evolution of super predator phenotypes is linked to
211 the constitutive activation of a predatory metabolic program, possibly via a constitutive
212 activation of the fatty acids β-oxidation pathway. Strikingly, the metabolic upshift observed in
213 the C10E9 strain is mitigated in the M1 strain, suggesting that metabolic fine-tuning was key
214 to the emergence of this phenotype (see Discussion).

215 **The WT strain but not the M1 strain experiences oxidative stress in the presence of prey**

216 In the evolved predator strains, the activation of the β-oxidation pathway could be expected to
217 be linked to the emission of Reactive Oxygen Species (ROS) (26), especially since the ETC
218 does not appear to be especially active to dissipate electrons from reducing species (Figure 4D).
219 This would be especially true in the C10E9 strain where the TCA also appears to be running at

high rate. Indeed, we observed by RNAseq that the expression of ROS-scavenging enzymes is highly upregulated, to extreme levels in the C10E9 strain, and to more moderate but still high levels in the M1 strain as compared to the WT (Figure 4E, quantified in Figure S7).
In contrast, the oxidative stress response was activated in the WT strain in the presence of prey but it was not the case in the M1 strain (Figure S6D and S8A-S7D). In the presence of prey, fatty acids β-oxidation, TCA and ETC genes were activated at high and comparable level in both strains (Figure S6A-S6C and S8A-S8C). This suggests that although the M1 strains experiences metabolic stress in pure culture, it is particularly well adapted to predation.

Increased resistance to oxidative stress is key to the enhanced predatory performance of the M1 strain

The results above suggest that the WT strain faces a higher level of oxidative stress than the M1 strain during predation. This could be explained for example if the constitutive expression of ROS scavenging enzymes in the M1 helps dissipate a ROS surge in the initial steps of predation. To test this, we introduced exogenous catalase to the medium and analyzed the relative predatory performance of WT and M1 in our assay. In the presence of catalase, the WT became just as efficient a predator as the M1, implying that heightened resistance to hydrogen peroxide H_2O_2, one of the three primary reactive oxygen species (ROS), plays a role in enhanced predatory performance (Figure 5A). Further supporting this observation, growth of the WT and M1 followed similar kinetics in the presence of exogenous catalase (Figure 5B).

In the M1 strain, the catalase *katB* gene is expressed 50-fold higher than in WT (Figure S8, SI Table 4), prompting examination of its role in predatory efficiency. As anticipated, the predatory capability of the Δ*katB* mutant diminished when contrasted with its M1 progenitor (Figure 5C). However, even with this reduction, the M1 Δ*katB* mutant outperformed the WT. This indicates that while *katB* induction contributes to enhanced predation, it is not the only factor. This might not be surprising given that other ROS detoxifying enzymes are also in the M1 strain (Figure 4E, Figure S7). Interestingly, deletion of *katB* in the WT strain had no effect on its predation showing that it only becomes important in the evolved M1 background (Figure S9).

To further underscore how ROS production hinders predatory capacities, we employed an *E. coli* Hpx mutant as prey. This mutant, devoid of three principal H_2O_2 scavenging enzymes (*katG*, *katE*, and *ahpC*), consequently accumulates H_2O_2 at substantial levels(27). Against this mutant, the predatory efficiency of the M1 diminished (Figure 5D). However, introducing exogenous catalase partially rescued this hyper-predation phenotype (Figure 5D). Under identical conditions, catalase supplementation only marginally enhanced the predation efficacy of the WT strain (Figure 5D).

Taken together, these observations confirm that during the predator-prey interaction, ROS present a significant hurdle for the predator. Enhanced resistance to ROS emerges as an important factor contributing to enhanced predation of the M1 strain.

ROS are generated by contact-dependent lysis

The advantage conferred by the constitutive expression of enzymes such as KatB in the M1 strain suggests that a possible ROS source might be the lysis of prey cells upon contact, for example as observed during Type-6 secretion-mediated killing(28).

When *E. coli* is used as prey, it does not seem to accumulate ROS on its own, as evidenced by the lack of induction (and even perhaps the downregulation) of ROS-responsive regulators and genes such as *soxS*, *oxyR*, *fur*, and *katG* (Figure S10). Consistent with this, *E. coli* cells pre-

265 labeled with CM-H2DCFDA, a general ROS probe which emits green fluorescence upon
266 oxidation(28, 29), were not fluorescent upon co-incubation with the predator. Interestingly,
267 upon *Myxococcus* contact-dependent killing, a sporadic fluorescence surge was occasionally
268 noticeable in *E. coli* cells adjacent to the lytic contact (Figure S11). This suggests that cell
269 rupture could discharge a ROS wave that impacts neighboring cells. However, this occurrence
270 was rarely observed, possibly due to the swift diffusion of ROS and its quasi-immediate dilution
271 in the extracellular environment.

272 Therefore, to definitively confirm that contact-induced lysis causes an oxidative surge, we
273 adopted two complementary strategies. In the first strategy, we used a *Myxococcus* strain in
274 which the Kil system remains functional but lacking the T3SS (Δ*t3ss*). This strain induces prey
275 cell death through plasmolysis, but without cell rupture(12). We postulated that if contact-
276 dependent killing produces ROS, then ROS buildup should be observable in prey targeted by
277 the Δ*t3ss Myxococcus* mutant. As shown in Figure 5E, CM-H2DCFDA-laden *E. coli*
278 manifested fluorescence following contact with *Myxococcus* cells, indicating a ROS burst.

279 In the second strategy, we engineered a novel killing assay within microdroplets (Figure S12
280 for methodological details). This setting provides a confined µm-sized compartment where
281 CM-H2DCFDA dilution is limited and thus allows detection of ROS production. Notably, when
282 CM-H2DCFDA-labeled *E. coli* cells were co-incubated with *Myxococcus* WT strain, a time-
283 dependent fluorescence enhancement was detected within the droplet (Figure 5F). Crucially,
284 this effect was reliant on contact-induced killing since significantly less fluorescence was
285 measured when a Δ*kil* mutant was used.

286 Conclusively, Kil-mediated contact-dependent killing produces an oxidative burst, which could
287 impose stress on predator cells. This might elucidate, at least in part, the superior performance
288 of the M1 variant, in which the predator cells are already primed with ROS-scavengers
289 production.

290 Discussion

291 Despite growing evidence that bacterial predators are ubiquitous in the environment, little is
292 known about the mechanisms by which they interact and consume their prey. Evolution
293 experiments have the potential to reveal critical features of predator-prey interactions,
294 mechanisms of prey resistance, as well as specific genes involved in predator prey
295 interactions(30–33). In a seminal study, Nair and Velicer conducted a co-evolution experiment
296 where both predator and prey (*E. coli*) were observed to co-adapt via accelerated genomic
297 evolution specific to each species(33). Remarkably, they observed the parallel evolution of
298 predator (*eatB*) and prey (*ompT*) loci, suggesting that these genetic traits are important in
299 predator-prey interaction.

300 In this study, we did not allow the prey to evolve and concentrated on the selection of enhanced
301 predatory phenotypes. This approach revealed that augmented predatory phenotypes can
302 emerge through metabolic adaptations. Specifically, we find that the M1 (and similarly the
303 C10E9 variant) is a more efficient predator at least in part because *katB* and other oxidative
304 stress response genes are constitutively expressed at high levels. However, this adaptation did
305 not emerge simply from activation of oxidative stress response genes but it likely finds its
306 source in a deep metabolic redirection toward fatty acids beta-oxidation as a major pathway for
307 energy production.

308 The importance of fatty acids beta-oxidation during predation (observed with all three preys)
309 suggests that prey-derived lipids are central to predator nutrition. We therefore propose that the
310 C10E9 and the M1 strains have adopted a specialized metabolism, burning lipids constitutively.
311 Because this metabolism creates oxidative stress in the absence of prey, the ROS response
312 pathway is turned on, which primes *Myxococcus* for its encounter with the prey. This scenario
313 is reinforced by the mutations that occurred during the evolutionary path to the M1 phenotype.
314 It is remarkable that the key mutations map to enzymes predicted to perform opposing reactions,
315 ACOL supplies Acetyl-CoA pools, while ACOT acts oppositely, either liberating CoA from
316 Acetyl-CoA or from long Acyl-CoA chains(25, 34). Thus, there were potentially two critical
317 steps that led to the M1 phenotype, a first mutation that could have deactivated the acetate
318 metabolism and increased activity of Fatty Acids degradation and the TCA cycle as a
319 compensatory mechanism at the cost of high oxidative stress (C10E9), and a second mutation
320 that mitigated that stress by slowing down the flow of Acetyl-CoA. Of note, while the CytC
321 mutation does not contribute on its own to the predation advantage, its presence is also
322 associated to the M1 phenotype. The functional association between ACOT and CytC will need
323 to be further defined, but clearly ACOT is essential for predation, suggesting that the regulation
324 of Acetyl-CoA fluxes is critical during this growth phase.

325 Oxidative stress is an important barrier to predation and it can come both from the predator
326 metabolism and prey lysis. In the M1 strain, the oxidative stress response remains at a low level
327 suggesting that the metabolic ROS can be effectively dissipated by the ETC (which is turned
328 on, Figure S7B). However, KatB is essential for the M1 phenotype. Thus, the ROS burst
329 experienced in contact with prey cells is a major stress for the predator.

330 We demonstrate that ROS are produced upon contact dependent lysis. However, the prey cells
331 do not produce ROS endogenously during predation because when they are stained with CM-
332 H2DCFDA, fluorescence is only observed following lysis and we did not observe induction of
333 ROS-responsive genes during predation (i.e., *katG, fur, soxS, oxyR*). A similar situation has
334 been described when *E. coli* is being attacked by Type-6 secretion system T6SS, another mode
335 of contact-dependent killing and the ROS source was not identified (28). Kil- or T6SS-
336 dependent effectors could generate ROS directly or indirectly, as the rupture prey membrane
337 integrity could also release electrons. Whichever the source, the results suggest that pathogens
338 or predators that kill by contact must adapt to the stress provoked by lysis of the target cell.

339 In conclusion, this study shows that general predators with higher predation capacities can be
340 readily selected in laboratory context. Interestingly, the metabolic changes observed in the
341 evolved strains echo emerging research suggesting that the fatty acid degradation pathway
342 might enhance bacterial stress responses, thereby better equipping them to navigate challenging
343 environments(35). The study was performed in a laboratory setting, which could limit the
344 ecological implications. Indeed, the M1 genotype might carry additional constraints that could
345 prevent the emergence of this particular variant in more natural habitats. But it is also possible
346 that wild-type strain became more adapted to prey-independent growth through domestication
347 and prolonged cultivation in nutrient-rich media. Nevertheless, the findings imply that a
348 spectrum of predatory phenotypes can emerge in response to specific environmental conditions.
349 In the future, the sequencing of wild strains directly sampled from the soil environment would
350 provide valuable insights into the occurrence of mutations akin to those observed in the M1
351 strain.

352 Acknowledgements

We would like to thank Benjamin Ezraty for the gift of the *E. coli* Hpx mutant strain and helpful discussions; Emma Bouveret for helpful discussions and help with fatty acids metabolism gene annotation; Julien Herrou for initial discussions at the beginning of the project and help with experiments; Swapnesh Panigrahi for helping with image analysis. Guilhem Chenon for assistance in setting up the droplet-based assays; Beatrice Py, Corinne Aubert and Mathieu Sourice for fruitful discussions. Sophie Helaine for helpful comments on the manuscript.

Funding: This work was supported by CNRS, Aix-Marseille University, the European Research Council (ERC) grant JAWS 885145. R.J. was supported by the Centuri Grant and ERC JAWS. N.-H.L was supported by the Fondation pour la Recherche Médical (FRM) grant ARF202110013986. J.Ba. and J.Bi. received the support of "Institut Pierre-Gilles de Gennes" (Laboratoire d'Excellence, "Investissements d'Avenir" program ANR-10-IDEX-0001-02 PSL, ANR-10-EQPX-34 and ANR-10-LABX-31). **Author contributions:** Conceived and designed the experiments: R.J., N.-H.L., B.H. and T.M.. Performed the experiments: R.J., N.-H.L., L.B., J.Ba. and J.Bi.. Analyzed the data: R.J., N.-H.L., L.B., Y.D., B.H., and T.M.. Wrote the paper: R.J., N.-H.L., and T.M. All authors commented on the manuscript. **Competing interests:** All other authors declare that they have no competing interests. **Data and materials availability:** All data needed to evaluate the conclusions in the paper are present in the paper and/or the Supplementary Materials. Additional data related to this paper may be requested from the authors.

METHODS:

Bacterial strains and growth conditions:

M. xanthus DZ2 strains were cultivated in Casitone Yeast Extract (CYE) medium, while *E. coli* MG1655 and *B. subtilis* strain 168 cells were grown in Luria-Bertani (LB) broth. The *C. crescentu*s strain NA1000 was cultured in PYE (Peptone Yeast Extract). All of the strains were grown at 32°C and the experiments were performed on 1.5% hard agar plates.

Effect of glucose concentration on predation:

M. xanthus and *E. coli* were cultured overnight in 20mL of their respective growth media at 32°C. On the following day, the cells were collected by centrifugation and resuspended in CF medium (comprising MOPS 10 mM at pH 7.6, KH2PO4 1 mM, MgSO4 8 mM, (NH4)2SO4 0.02%, Na citrate 0.2%, and Bacto Casitone 0.015%). The OD600 of both cultures was adjusted to 5. Subsequently, 10 µL of the *E. coli* suspension was carefully deposited alongside 10 µL of the *M.xanthus* suspension onto separate CF agar plates, each with varying glucose concentrations (0%, 0.075%, 0.1%, and 0.2%). Once the drops had air-dried, the plates were incubated at 32°C, and observations were made after a 72-hour incubation period (Figure 2A).

Evolution experiment:

E. coli was grown overnight in 20 mL of LB at 32°C. The following day, the cells were pelleted and resuspended in CF medium with the OD600 adjusted to 5. 20 µL of this suspension was then placed on a CF 1.5% agar plate containing 0.075% glucose. After the drop had dried, *M. xanthus* cells (previously grown on CYE agar plates at 32°C) were added to the center of the E. coli drop using a sterilized pipette tip. After about 6 days, when the *M. xanthus* cells had consumed all of the *E. coli* and reached the edge of the *E. coli* colony, they were removed from the edge of the colony and transferred to a new 20 µL *E. coli* drop (Figure 2B). This cycle was repeated 20 times, and after every 5 cycles, the concentration of glucose in the CF agar was increased by 10% of the previous concentration. Additionally, after each 10 cycles, a DMSO stock of the evolved *M. xanthus* was prepared.

Construction of *M. xanthus* mutant strains:

All primers, plasmids and strains used for this study are listed in Tables S5-S7. Gene deletions and point mutations in *M. xanthus* were achieved using a double-recombination approach as described previously(36). In brief, sequences ranging from 800 to 1000 nucleotides flanking the targeted genes for deletion (or the point mutations for insertion) were PCR amplified and assembled into the pBJ114 suicide plasmid (GalS, KanR) via Gibson assembly. This plasmid was then electroporated into *M. xanthus*. Following successive selections with Kanamycin and Galactose, clones harboring the desired genetic modifications were identified using PCR.

Predation killing assay:

Myxococcus and kanamycin-resistant strains of the prey (*E. coli*, *B. subtilis*, or *C. crescentu*s) were grown overnight in 20 mL of their respective rich media at 32C. Cells were pelleted and the OD600 of *Myxococcus* and prey was adjusted to 1 and 5, respectively, in CF medium. The *Myxococcus* and prey were mixed in a 1:3 ratio, and a 10 µL drop of this mixture was placed

415 on a CF 1.5% agar plate containing 0.075% glucose. After 24 hours, cells from the spot were
416 harvested and the colony forming units of prey were counted on Kanamycin-supplemented LB
417 media for *E. coli* and *B. subtilis*, and on PYE supplemented with Kanamycin media for *C.*
418 *crescentus*. Each assay is performed in technical duplicate.
419
420 **Growth Curve Determination of M. xanthus via Digital PCR (dPCR):**
421 To assess the growth of *M. xanthus* during *E. coli* predation on CF agar media, we employed
422 droplet digital PCR (dPCR) to directly quantify its genomic DNA concentration, using it as a
423 surrogate measure for growth. Genomic DNA was extracted from three pooled killing assay
424 spots (as detailed in the previous section) utilizing the Monarch® Genomic DNA Purification
425 Kit (NEB). Quantification of genomic DNA copies was targeted at the *kdpAB* gene and carried
426 out with the Naica® Crystal Digital PCR System using Sapphire chips (Stilla Technologies).
427
428 The dPCR reactions consisted of PerfeCta® qPCR ToughMix® UNG (Quantabio), 0.8 ng/µL
429 Alexa 647 (Invitrogen), 1.5X EvaGreen® (Biotium), 4% DMSO (Biolabs), 200 nM of each
430 primer *kdpAB*(37), and 10 µL of the DNA template. Amplification was performed on the Geode
431 thermocycler (Stilla Technologies) under the following conditions: an initial 95˚C for 3
432 minutes, succeeded by 45 cycles of 95˚C for 10 seconds and 60˚C for 15 seconds. Fluorescence
433 acquisition was accomplished using the Prism3 imager and Crystal Reader software (Stilla
434 Technologies), with data analysis conducted via the Crystal Miner software (Stilla
435 Technologies).
436
437 **RNAseq library preparation and data analysis:**
438 *M. xanthus* strains were grown in 20mL of CYE, while *E. coli* and *B. subtilis* cells were cultured
439 in 20mL of LB. The *C. crescentu*s was grown in 20mL of PYE. All of the strains were grown
440 at 32°C overnight. The next day, the cells were pelleted and the growth media was removed.
441 The cells were resuspended in CF medium such that the OD600 of *M. xanthus* was adjusted to
442 5, while the OD600 of the prey bacteria was adjusted to 10. *M. xanthus* and prey bacteria were
443 mixed in a 1:3 ratio, and 20 µL of this mixture was spotted onto a CF 1.5% agar plate containing
444 0.075% glucose. For the *Myxococcus* alone condition, an *M. xanthus* culture with an OD600 of
445 5 was mixed with CF medium in a 1:3 ratio. The plate was incubated at 32°C. After ~2 hours,
446 cells from 25 of the spots were collected using sterile loops, combined to form a single sample,
447 and rapidly frozen in liquid nitrogen for storage at -80°C. To extract RNA, the cells were lysed
448 using lysozyme (10 mg/mL) and then the RNA was extracted using the TRiZol (Invitrogen)
449 protocol. The total RNA was treated with TURBO™ DNase (Invitrogen), and the quantity and
450 quality of the RNA was measured using a Qubit and a TapeStation, respectively. Libraries were
451 prepared using 1 µg of total RNA according to the Zymo-Seq RiboFree Total RNA Library Kit
452 protocol. The quantity and quality of the libraries were also measured using a Qubit and a
453 TapeStation. The libraries were sequenced on an Illumina NextSeq500 platform at TGML in
454 Marseille, generating approximately 10-35 million 75 bp paired-end reads per sample. The
455 reads were mapped to the *M. xanthus* DK1622 genome (GCF_000012685.1, NCBI) using
456 Burrows-Wheeler Aligner (version 0.7.10)(38) default parameters and the number of reads
457 mapping to each coding sequence (CDS) was counted using HTseq (version 0.6.1)(39). The
458 read counts were then normalized utilizing the DEseq2 method(40), and genes exhibiting

459 differential expression were identified with a p-adjusted value <0.05 using the Wald test in
460 DEseq2. Gene ontology enrichment analysis was performed on differentially expressed genes
461 using *clusterprofiler* 4.0 package(41) in R. The normalized read counts from DEseq2 were
462 further utilized to create heatmaps illustrating gene expression patterns (Figure 4). To
463 accomplish this, the DEseq2 normalized read counts were individually scaled for each gene
464 across various conditions using the scale function in R. These scaled values were then plotted
465 using the *pheatmap* function in R. The genes related to beta-oxidation, the TCA cycle, the
466 Electron Transfer Chain, and ROS response, as shown in heatmaps, were annotated using a
467 combination of the KEGG database, literature search, and a manual homology search to identify
468 *E. coli* homologs within the *Myxococcus* genome.
469
470 **RT-qPCR analysis:**
471 RNAs were prepared from pooled 40 killing assay spots (as detailed in the previous section) at
472 2h post-incubation. The cells were harvested and flash frozen at -80°C. Total RNAs were
473 isolated from the pellet using the Maxwell® 16 LEV miRNA Tissue Kit (Promega) according
474 to the manufacturer's instructions and an extra TURBO DNase (Invitrogen) digestion step to
475 eliminate the contaminating DNA. The RNA quality was assessed by the TapeStation system
476 (Agilent). RNA was quantified spectrophotometrically at 260 nm (NanoDrop 2000C; Thermo
477 Fisher Scientific). For cDNA synthesis, 1 µg total RNA and 0.5 µg random primers (Promega)
478 were used with the GoScript™ Reverse transcriptase (Promega) according to the manufacturer
479 instruction.

480 Quantitative real-time PCR (RT-qPCR) analyses were performed on a CFX96 Real-Time
481 System (Bio-Rad). The reaction volume was 15 µL and the final concentration of each primer
482 was 0.5 µM. The cycling parameters of the RT-qPCR were 98°C for 2 min, followed by 45
483 cycles of 98°C for 5 s, 58°C for 10 s, 72°C for 1s. A final melting curve from 65°C to 95°C is
484 added to determine the specificity of the amplification. To determine the amplification kinetics
485 of each product, the fluorescence derived from the incorporation of SybrGreen into the double-
486 stranded PCR products was measured at the end of each cycle using the SsoAdvanced Universal
487 SYBR Green Supermix 2X Kit (Bio-Rad, France). The results were analyzed using Bio-Rad
488 CFX Maestro software, version 1.1 (Bio-Rad, France). The rRNA16S gene and dnaK gene were
489 used as a combined reference for normalization. The amplification efficiencies for each primer
490 pair were between 80 and 100%.

491 **DNAseq library preparation and data analysis:**
492 *M. xanthus* strains were grown in 20mL of CYE at 32°C overnight. The next day, 500uL of the
493 cultured cells were pelleted and the growth media was removed. DNA was extracted using the
494 Master Pure DNA purification kit (Cat No. 85200) from Epicentre. NEBNext® Ultra™ II DNA
495 Library Prep Kit for Illumina® (NEB #E7645S/L) was used for library preparation and libraries
496 were sequenced on Illumina MiSeq or NextSeq 2000 platform and more than 1.25M read pairs
497 of 150bp length were generated per sample i.e. more than 40X coverage for *M.xanthus* DZ-2
498 genome. SNPs were detected using breseq version 0.35.1(42).
499
500 **Fluorescence Microscopy of ROS Accumulation in *E. coli* during *M. xanthus* Predation:**

501 *E. coli* prey and *M. xanthus* predator strains were cultured overnight in their designated media.
502 The *E. coli* culture was subsequently grown to an OD600 of 2 at 37°C using LB supplemented
503 with 20 µM CM-H2DCFDA, an ROS-sensitive dye. After centrifugation, cells were
504 resuspended in CF medium to an OD600 of 2. Equal aliquots of these suspensions were mixed
505 and 1 µl was spotted onto a fresh CF 1% agarose pad on a microscope slide. Following a brief
506 drying period and incubation in the dark at room temperature for 30 minutes, imaging was
507 performed. The TE2000-E-PFS (Nikon) inverted epifluorescence microscope, equipped with a
508 ×100/1.4 DLL objective and Nikon's NIS software, was used. Time-lapse recordings of 30
509 minutes (capturing every 20 seconds) were conducted at x100 magnification. DIA images
510 utilized a 20 ms light exposure, while GFP images required a 100 ms fluorescence exposure
511 with a 30% power intensity at an excitation wavelength of 470 nm, ensuring minimized photo-
512 bleaching and phototoxicity. The 'Perfect Focus System' (PFS) was engaged throughout for
513 consistent focus.
514
515 **Droplet microfluidic & Image analysis:**
516 *M.xanthus* and *E. coli* cells were cultured overnight at 32°C in their respective rich media.
517 Subsequently, the *E. coli* cells were further cultivated for 4 hours at 37°C in LB supplemented
518 with 20µM CM-H2DCFDA. Following the growth period, cells were harvested through
519 centrifugation and subsequently resuspended in CF medium. The *E. coli* suspension was
520 adjusted to an OD600 of 2, while the *M.xanthus* suspension was set to an OD600 of 7 (Figure
521 5F). These distinct cell suspensions in CF media were introduced into separate sample inlets,
522 along with another inlet for HFE7500 oil containing 2% weight of FluoroSurfactant (RAN
523 Biotechnologies, MA 01915), within a custom-designed droplet chip at ESPCI(43) (Figure
524 S12). Both CF and oil phases were drawn through orthogonal channels inside the chip,
525 accomplished by generating a vacuum within the chip using a 5 mL syringe pump. This
526 specialized chip facilitated the creation of thousands of uniformly sized droplets, each with a
527 volume of around 80pL, utilizing the introduced cell cultures. These droplets consisted of CF
528 media suspended within an oil medium, establishing a water-in-oil droplet configuration. Each
529 of these droplets contained a mixture of both *M. xanthus* and *E. coli* cells, with approximately
530 20 cells of each type present in every droplet. This cell composition was determined based on
531 the previously specified OD values, i.e. OD600 of 2 for *E. coli*, while OD600 of 7 for the
532 *M.xanthus* suspension.
533
534 After the generation of droplets, they were pulled into a chamber with a consistent height of
535 30µm, causing the droplets to undergo deformation into a flattened, pancake-like configuration.
536 This compression facilitated their observation under a microscope. The compressed droplets
537 exhibited an approximate diameter of 40µm. These droplets were then subjected to imaging
538 using an inverted epifluorescence microscope, specifically the TE2000-E-PFS by Nikon,
539 operating at a 20x magnification. At this magnification level, each image frame could
540 encompass approximately 700 droplets. A series of time-lapse recordings were performed,
541 spanning a 15-hour duration, with images captured at 20-minute intervals throughout this
542 period. To extract meaningful data from these images, a segmentation process was applied to

delineate individual droplets, and subsequent analysis was carried out using ImageJ. This analysis aimed to calculate the mean intensity for each individual droplet.

Statistical Analysis:

Statistical analyses were performed using GraphPad Prism 10 (GraphPad Software Inc., La Jolla, CA) and R. Prism 10 was used to determine statistical significance. Non-parametric Mann-Whitney tests were used to compare ranks between two conditions. One-way ANOVA analysis with post-hoc multiples comparison using the Dunnett test were used on datasets with 3 or more conditions.

Data Availability:

The raw transcriptome sequencing data, in the form of raw-reads, has been deposited in the NCBI Sequence Read Archive (SRA) with the Bioproject accession number: PRJNA1040215.

References

1. R. S. Meena, *et al.*, Impact of Agrochemicals on Soil Microbiota and Management: A Review. *Land 2020, Vol. 9, Page 34* **9**, 34 (2020).
2. A. Barros-Rodríguez, P. Rangseekaew, K. Lasudee, W. Pathom-Aree, M. Manzanera, Impacts of Agriculture on the Environment and Soil Microbial Biodiversity. *Plants 2021, Vol. 10, Page 2325* **10**, 2325 (2021).
3. L. Seabrook, C. A. Mcalpine, M. E. Bowen, Restore, repair or reinvent: Options for sustainable landscapes in a changing climate. *Landsc Urban Plan* **100**, 407–410 (2011).
4. S. Thiery, C. Kaimer, The Predation Strategy of Myxococcus xanthus. *Front Microbiol* **11**, 513035 (2020).
5. B. A. Hungate, *et al.*, The functional significance of bacterial predators. *mBio* **12** (2021).
6. Y. Zhou, X. Zhang, Q. Yao, H. Zhu, microorganisms Both Soil Bacteria and Soil Chemical Property Affected the Micropredator Myxobacterial Community: Evidence from Natural Forest Soil and Greenhouse Rhizosphere Soil (2020) https:/doi.org/10.3390/microorganisms8091387 (November 13, 2023).
7. S. Petters, *et al.*, The soil microbial food web revisited: Predatory myxobacteria as keystone taxa? *ISME J* **15**, 2665–2675 (2021).
8. V. Groß, A. Reinhard, S. Petters, M. Pichler, T. Urich, Adding complexity to soil food webs: Myxobacteria have broad predation spectra with bacteria, yeasts and filamentous fungi in vitro. *Eur J Soil Biol* **117**, 103508 (2023).
9. P. G. Livingstone, R. M. Morphew, D. E. Whitworth, Myxobacteria are able to prey broadly upon clinically-relevant pathogens, exhibiting a prey range which cannot be explained by phylogeny. *Front Microbiol* **8**, 285257 (2017).
10. C. T. Bull, K. G. Shetty, K. V. Subbarao, Interactions Between Myxobacteria, Plant Pathogenic Fungi, and Biocontrol Agents. *https://doi.org/10.1094/PDIS.2002.86.8.889* **86**, 889–896 (2007).
11. S. Seef, *et al.*, A Tad-like apparatus is required for contact-dependent prey killing in predatory social Marseille and Turing Center for Living Systems. *denotes equal contribution. *bioRxiv*, 2021.02.25.432843 (2021).
12. S. Thiery, P. Turowski, J. E. Berleman, C. Kaimer, The predatory soil bacterium Myxococcus xanthus combines a Tad- and an atypical type 3-like protein secretion system to kill bacterial cells. *Cell Rep* **40** (2022).
13. A. Konovalova, T. Petters, L. Søgaard-Andersen, Extracellular biology of Myxococcus xanthus https:/doi.org/10.1111/j.1574-6976.2009.00194.x (November 14, 2023).
14. S. Seef, *et al.*, A tad-like apparatus is required for contact-dependent prey killing in predatory social bacteria. *Elife* **10** (2021).
15. A. D. Morgan, R. C. MacLean, K. L. Hillesland, G. J. Velicer, Comparative analysis of myxococcus predation on soil bacteria. *Appl Environ Microbiol* **76**, 6920–6927 (2010).
16. P. G. Livingstone, R. M. Morphew, D. E. Whitworth, Myxobacteria are able to prey broadly upon clinically-relevant pathogens, exhibiting a prey range which cannot be explained by phylogeny. *Front Microbiol* **8**, 285257 (2017).
17. C. Wang, *et al.*, Comparative genomics and transcriptomics insight into myxobacterial metabolism potentials and multiple predatory strategies. *Front Microbiol* **14**, 1146523 (2023).
18. J. Pérez, F. J. Contreras-Moreno, J. Muñoz-Dorado, A. Moraleda-Muñoz, Development versus predation: Transcriptomic changes during the lifecycle of Myxococcus xanthus. *Front Microbiol* **13** (2022).

19. P. G. Livingstone, A. D. Millard, M. T. Swain, D. E. Whitworth, Transcriptional changes when Myxococcus xanthus preys on Escherichia coli suggest myxobacterial predators are constitutively toxic but regulate their feeding. *Microb Genom* **4**, e000152 (2018).
20. S. Inouye, *et al.*, A Large Family of Eukaryotic-Like Protein Ser/Thr Kinases of Myxococcus xanthus, a Developmental Bacterium. *https://home.liebertpub.com/omi* **5**, 103–120 (2004).
21. B. F. Watson, M. Dworkin, Comparative Intermediary Metabolism of Vegetative Cells and Microcysts of Myxococcus xanthus. *J Bacteriol* **96**, 1465–1473 (1968).
22. F. Fiegna, S. Pande, H. Peitz, G. J. Velicer, Widespread density dependence of bacterial growth under acid stress https:/doi.org/10.1016/j.isci.2023.106952 (November 14, 2023).
23. M. Pérez-Burgos, *et al.*, Characterization of the Exopolysaccharide Biosynthesis Pathway in Myxococcus xanthus. *J Bacteriol* **202** (2020).
24. A. S. Reger, J. M. Carney, A. M. Gulick, Biochemical and crystallographic analysis of substrate binding and conformational changes in acetyl-CoA synthetase. *Biochemistry* **46**, 6536–6546 (2007).
25. Y. B. Khandokar, *et al.*, Structural insights into GDP-mediated regulation of a bacterial acyl-CoA thioesterase. *Journal of Biological Chemistry* **292**, 20461–20471 (2017).
26. M. Fasnacht, N. Polacek, Oxidative Stress in Bacteria and the Central Dogma of Molecular Biology. *Front Mol Biosci* **8**, 671037 (2021).
27. S. Park, X. You, J. A. Imlay, Substantial DNA damage from submicromolar intracellular hydrogen peroxide detected in Hpx- mutants of Escherichia coli. *Proc Natl Acad Sci U S A* **102**, 9317–9322 (2005).
28. T. G. Dong, *et al.*, Generation of reactive oxygen species by lethal attacks from competing microbes. *Proc Natl Acad Sci U S A* **112**, 2181–2186 (2015).
29. D. J. Dwyer, *et al.*, Antibiotics induce redox-related physi. *Proc Natl Acad Sci U S A* **111**, E2100 (2014).
30. V. Kaitala, T. Hiltunen, L. Becks, T. Scheuerl, Co-evolution as an important component explaining microbial predator-prey interaction. *J Theor Biol* **486**, 110095 (2020).
31. M. C. Duncan, *et al.*, High-throughput analysis of gene function in the bacterial predator bdellovibrio bacteriovorus. *mBio* **10** (2019).
32. N. Sydney, *et al.*, The Genetics of Prey Susceptibility to Myxobacterial Predation: A Review, Including an Investigation into Pseudomonas aeruginosa Mutations Affecting Predation by Myxococcus xanthus. *Microb Physiol* **31**, 57–66 (2021).
33. R. R. Nair, *et al.*, Bacterial predator-prey coevolution accelerates genome evolution and selects on virulence-associated prey defences. *Nat Commun* **10** (2019).
34. S. Zhang, *et al.*, Metabolic engineering for efficient supply of acetyl-CoA from different carbon sources in Escherichia coli. *Microb Cell Fact* **18**, 1–11 (2019).
35. K. Jaswal, M. Shrivastava, R. Chaba, Revisiting long-chain fatty acid metabolism in Escherichia coli: integration with stress responses. *Curr Genet* **67**, 573–582 (2021).
36. V. H. Bustamante, I. Martínez-Flores, H. C. Vlamakis, D. R. Zusman, Analysis of the Frz signal transduction system of Myxococcus xanthus shows the importance of the conserved C-terminal region of the cytoplasmic chemoreceptor FrzCD in sensing signals. *Mol Microbiol* **53**, 1501–1513 (2004).
37. P. G. Livingstone, A. D. Millard, M. T. Swain, D. E. Whitworth, Transcriptional changes when Myxococcus xanthus preys on Escherichia coli suggest myxobacterial predators are constitutively toxic but regulate their feeding. *Microb Genom* **4**, e000152 (2018).

38. H. Li, R. Durbin, Fast and accurate short read alignment with Burrows–Wheeler transform. *Bioinformatics* **25**, 1754–1760 (2009).
39. S. Anders, P. T. Pyl, W. Huber, HTSeq—a Python framework to work with high-throughput sequencing data. *Bioinformatics* **31**, 166–169 (2015).
40. M. I. Love, W. Huber, S. Anders, Moderated estimation of fold change and dispersion for RNA-seq data with DESeq2. *Genome Biol* **15**, 1–21 (2014).
41. T. Wu, *et al.*, clusterProfiler 4.0: A universal enrichment tool for interpreting omics data. *Innovation* **2** (2021).
42. D. E. Deatherage, J. E. Barrick, Identification of mutations in laboratory evolved microbes from next-generation sequencing data using breseq. *Methods Mol Biol* **1151**, 165 (2014).
43. K. Langer, N. Bremond, L. Boitard, J. Baudry, J. Bibette, Micropipette-powered droplet based microfluidics. *Biomicrofluidics* **12** (2018).
44. P. V. Troshin, J. B. Procter, G. J. Barton, Java bioinformatics analysis web services for multiple sequence alignment—JABAWS:MSA. *Bioinformatics* **27**, 2001–2002 (2011).

FIGURES:

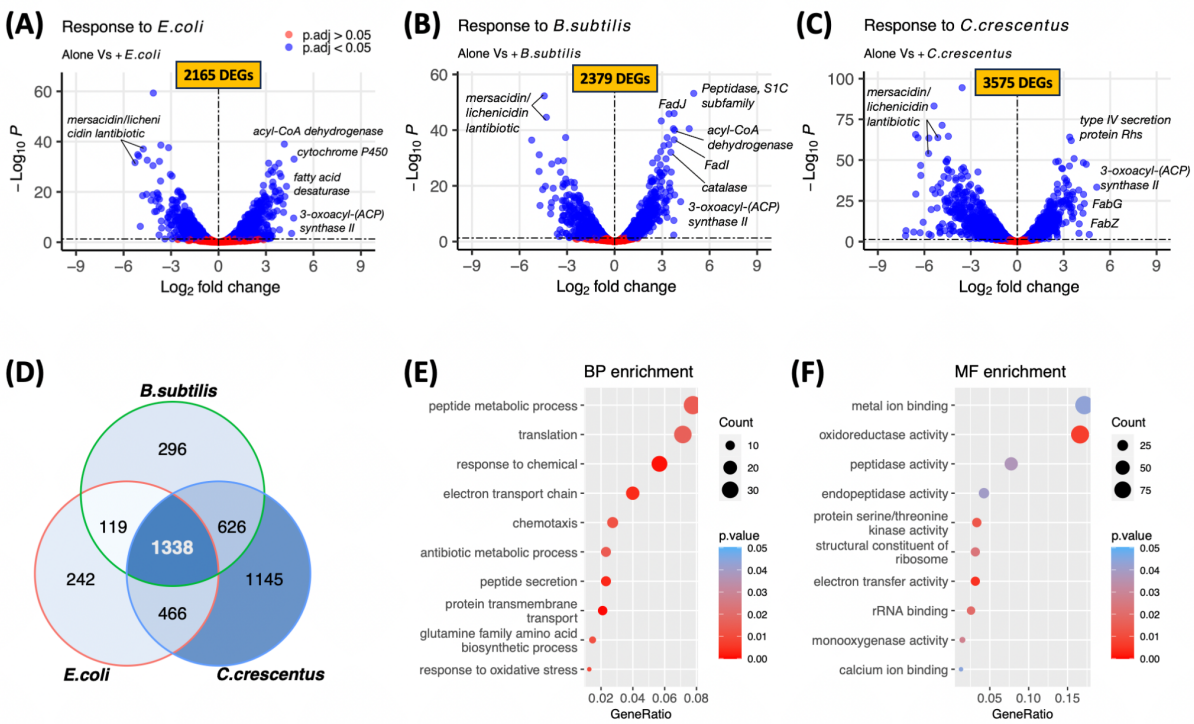

FIGURE 1: Transcriptomic shifts in wild-type *M.xanthus* in response to varied prey. **(A)** Contrasting gene expression patterns of *M.xanthus* between solitary state and *E. coli* predation (RNA-seq, n=3 biological replicates). Genes with a positive log2 fold change value are up-regulated in the *M.xanthus* + prey condition, while genes with a negative log2 fold change value are up-regulated in the solitary condition. DEGs stands for Differentially Expressed Genes ($p.adj < 0.05$, Wald test). **(B)** Gene expression variations in *M.xanthus* during solitary state versus *B. subtilis* predation (n=3). **(C)** Alterations in gene expression of *M.xanthus* during solitary state versus *C. crescentus* predation (n=3). **(D)** Common and distinct DEGs in *M.xanthus* predation across three distinct prey types. **(E)** Gene ontology term enrichment for biological processes in common genes linked to predation on all three prey. **(F)** Gene ontology term enrichment for molecular functions in common genes involved in predation on all three prey.

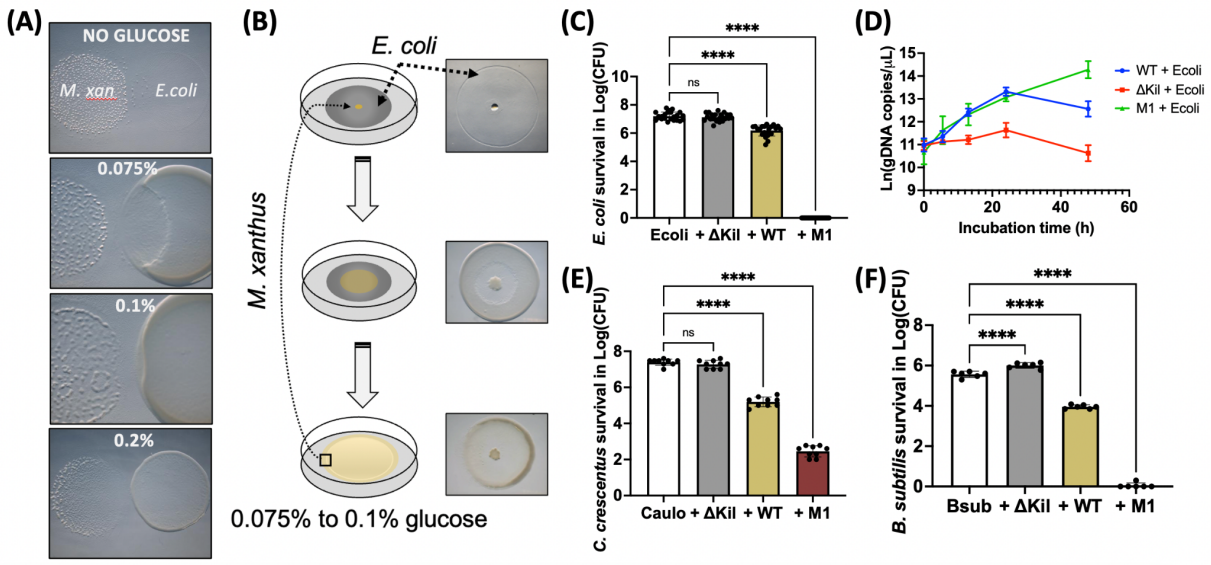

FIGURE 2: Evolution of a super predator from WT *M.xanthus*. (A) In a co-incubation experiment lasting 72 hours, *M. xanthus* and *E. coli* colonies were spotted newt to each other on CF media with varying glucose concentrations (ranging from 0% to 0.2%). The efficiency of *M. xanthus* predation decreases with increasing glucose concentrations. **(B)** During the evolution experiment, *M. xanthus* cells were placed in the center of an *E. coli* colony. As the *M. xanthus* cells consumed a significant portion of the *E. coli* population and reached the prey colony edge, they were transferred to the center of a new *E. coli* colony. After every 5 cycles, the glucose concentration in the media was gradually raised by 10%. **(C)** Killing assay of *E. coli* MG1655 prey using *M. xanthus* DZ2 WT, predation-deficient ΔKil, and evolved mutant M1 as predators. The bar graph shows the mean prey survival in log10(CFU) after a 24-hour coincubation +/- standard deviation (SD) derived from a minimum of 10 biological replicates. Statistical significance was determined using one-way ANOVA, with post-hoc multiple comparisons performed via the Dunnett test; ns: not significant, **** $p < 0.0001$. **(D)** Growth curves of *M. xanthus* DZ2 WT, predation-deficient ΔKil, and evolved mutant M1 during predation on *E. coli* prey. The scatter plot depicts Ln(gDNA copies/µL) across various predation time points. gDNA concentrations were directly quantified using digital PCR (dPCR). Error bars indicate the SD derived from 3 biological replicates. Comparison of WT and M1 predation efficiency on *B. subtilis* **(E)** and *C. crescentus* **(F)**, assessed by counting prey CFU after predation. The bar graph shows the mean prey survival in log10(CFU) after a 24-hour coincubation +/- SD derived from 3 biological replicates. Statistical significance was determined using one-way ANOVA, with post-hoc multiple comparisons performed via the Dunnett test; ns: not significant, **** $p < 0.0001$.

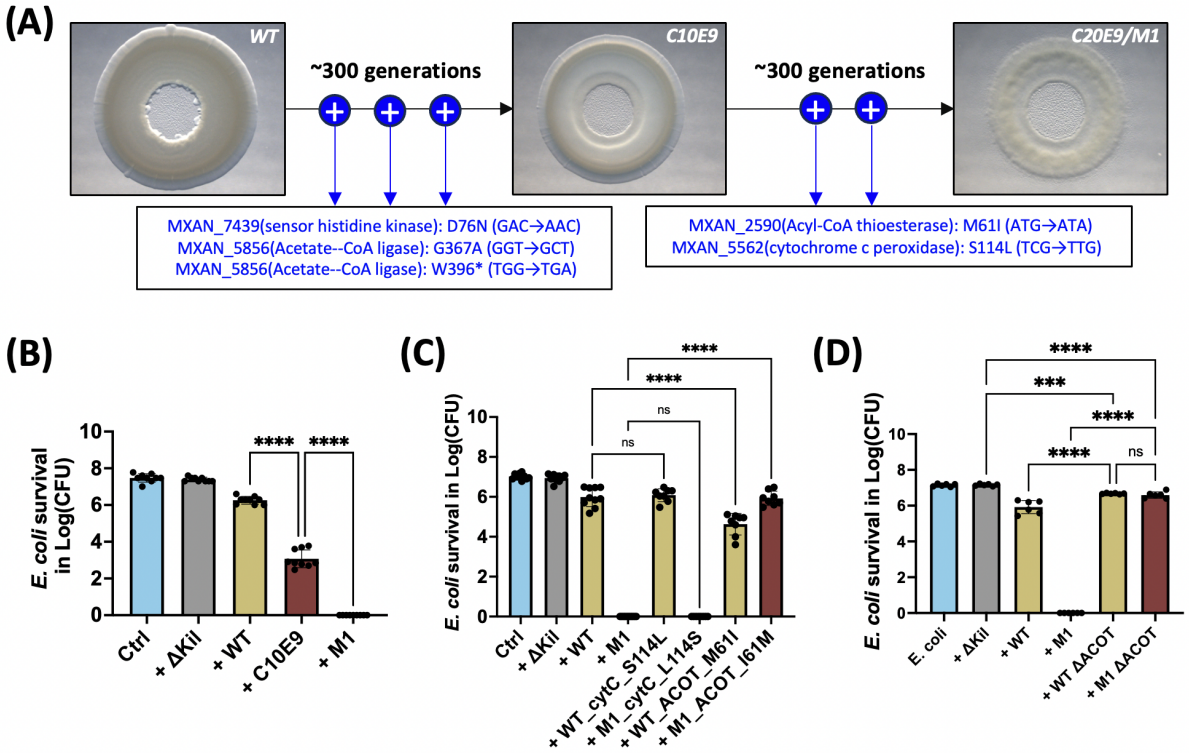

FIGURE 3: SNPs associated with efficient predation. (A) Genome sequencing revealed that the M1(C20E9) strain emerged after selection of an intermediate C10E9 strain. The WT ancestor differs from the C10E9 by 3 SNPs. Two additional SNPs separate the C10E9 transition from the M1. **(B)** Predation efficiency of the evolutionary intermediate C10E9 on *E. coli*. C10E9 exhibits an intermediate predation efficiency, situating between the killing capacities of WT and M1 strains when targeting *E. coli* prey. **(C)** Influence of point mutations on the predation phenotype of *M. xanthus* strains. *E. coli* prey was subjected to predation by *M. xanthus* WT strains with introduced point mutations: S114L in CytC or M61I in ACOT, as well as M1 strains where these individual point mutations were reverted. **(D)** Impact of ACOT gene deletion on predation efficiency of WT and M1 strains. The deletion of the ACOT gene from both strains resulted in diminished predation efficiency, suggesting that the SNP present within the M1 ACOT gene may be conferring a gain-of-function effect. All the bar graphs show the mean *E. coli* survival in log10(CFU) after a 24-hour coincubation with different predator strains +/- SD derived from a minimum of 3 biological replicates. Statistical significance was determined using one-way ANOVA, with post-hoc multiple comparisons performed via the Dunnett test; *ns*: not significant, *** $p < 0.001$, **** $p < 0.0001$.

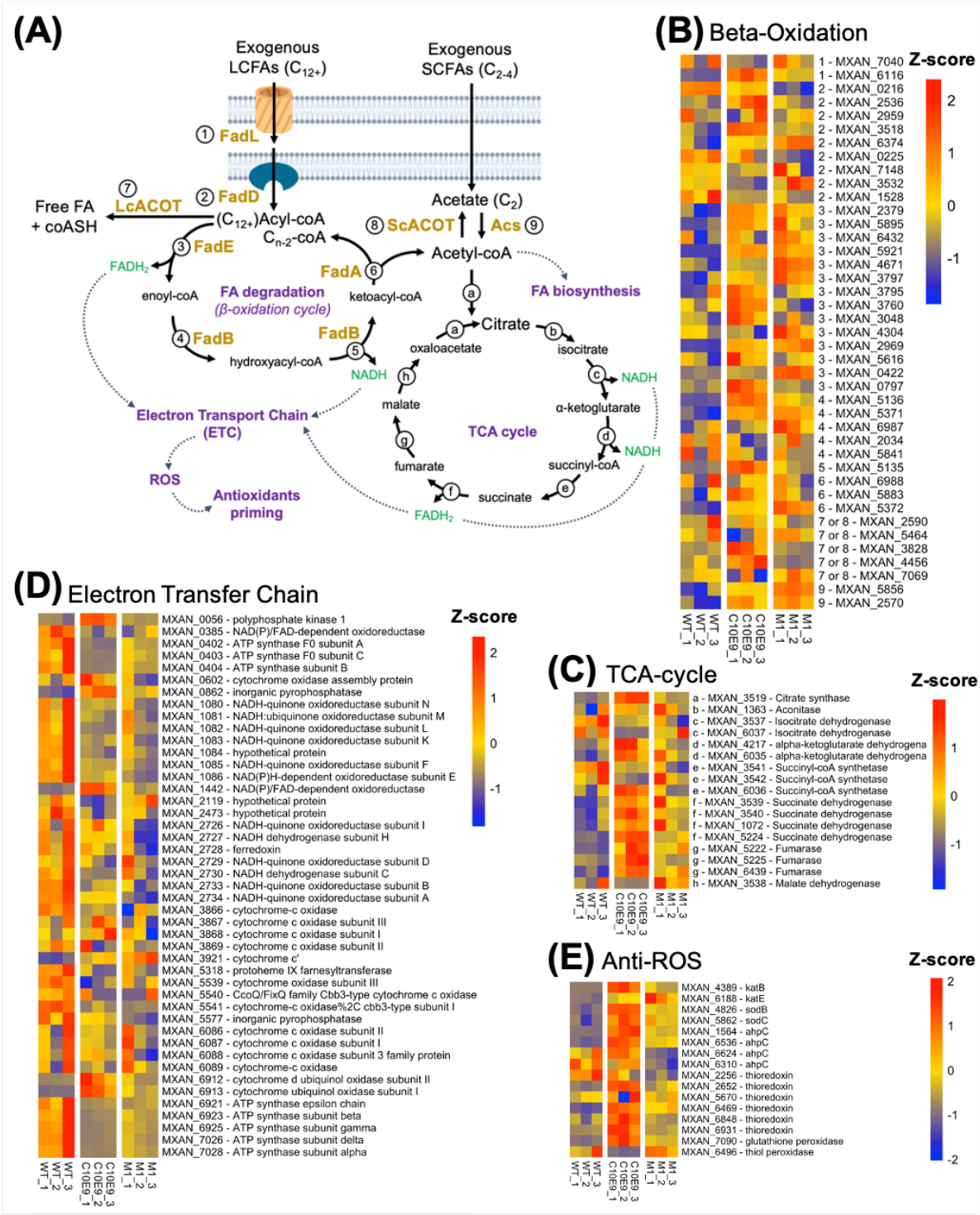

Figure 4: Metabolic Adaptation Mechanisms in Predator Mutants. (A) Predicted Exogenous FA-degradation pathway based on *Myxococcus* genome annotation. Long-Chain Fatty Acids (LCFAs, ≥ C12) are imported via the FadL transporter (1), while Short-Chain Fatty Acids (SCFAs, e.g., Acetate) diffuse directly across the membrane. LCFAs are activated by acyl-CoA synthase FadD (2) and subsequently undergo β-oxidation through enzymes FadE (Acyl-CoA dehydrogenase, 3), FadB (Enoyl-CoA hydratase and Hydroxyacyl-CoA dehydrogenase, 4 and 5), and FadA (Ketoacyl-CoA thiolase, 6), producing NADH and FADH2. In contrast, Acetate is directly activated to Acetyl-CoA by Acetate-coA synthetase (9). Long-

734 chain Acyl-CoA and Acetyl-CoA are deactivated by Long chain Acyl Thioesterase LcACOT
735 and Short chain acyl-CoA ScACOT respectively (7 and 8). Acetyl-CoA enters both fatty acid
736 biosynthesis and the TCA cycle, generating NADH and FADH2 for the Electron Transfer Chain
737 (ETC). Depending on ETC activity, electron overflow can occur, leading to ROS production.
738 High ROS levels initiate oxidative stress pathways, enhancing antioxidant production and
739 modulating iron homeostasis. **(B-E)** Heatmap representations of gene expression profiles of
740 genes annotated to be involved in Fatty acid β-oxidation (B), TCA cycle (C); Electron Transfer
741 Chain (D) and Antioxidant defense (E). Numbers preceding the gene MXAN accession
742 numbers indicate their functional annotation with respect to the cycle shown in (A). Strains
743 compared: DZ2 WT, C10E9, and M1. Each column within the heatmaps represents an
744 independent biological replicate. The values shown in the heatmaps represent DESeq2-
745 normalized counts that have been scaled across conditions for each gene. This scaling allows
746 for the visualization of expression level changes for multiple genes simultaneously. However,
747 it's important to note that this scaling does not accurately represent the actual fold change
748 differences between conditions.

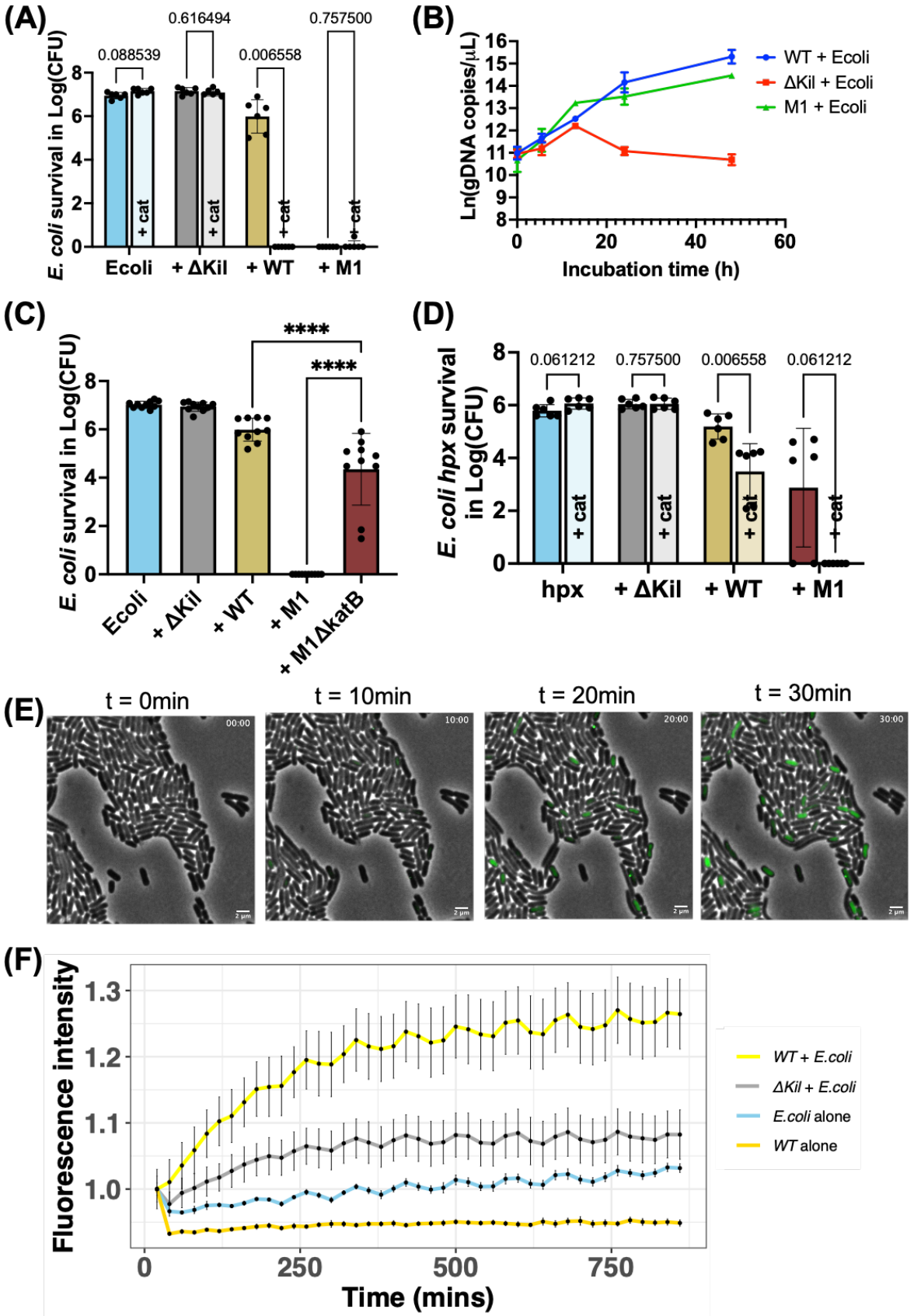

FIGURE 5: ROS adaptation explains the M1 phenotype. (A) Influence of catalase addition on the predation of *E. coli* MG1655 by *M. xanthus* DZ2 strains. The bar graph illustrates the mean survival of E. coli MG1655 in log10(CFU) after a 24-hour coincubation with M. xanthus DZ2 WT, predation-deficient ΔKil, and evolved mutant M1 predators, in the presence or

754 absence of exogenously added catalase (5ug/ml). Each bar denotes the mean +/- SD from 3
755 biological replicates. Pairwise statistical comparisons were made using Mann-Whitney tests,
756 with *p*-values indicated on the graph. **(B)** Growth curves of *M. xanthus* DZ2 WT, predation-
757 deficient ΔKil, and evolved mutant M1 during predation on E. coli prey in the presence of
758 5ug/ml catalase. The scatter plot depicts the natural log-transformed gDNA copies/μL across
759 various predation time points. gDNA concentrations were directly quantified using digital PCR
760 (dPCR). Error bars indicate the SD derived from 3 biological replicates. **(C)** Deletion of *katB*
761 in M1 diminishes its predation efficiency. The bar graph presents the average survival of *E. coli*
762 MG1655, expressed in log10(CFU), after a 24-hour coincubation with various *M. xanthus* DZ2
763 predators: WT, predation-deficient ΔKil, evolved mutant M1, and a *katB*-deleted variant of M1.
764 Each bar represents mean +/- SD derived from 3 biological replicates. Statistical significance
765 was determined using one-way ANOVA, with subsequent multiple comparisons conducted
766 using the Dunnett test; **** $p < 0.0001$. **(D)** Enhanced resistance to *M. xanthus* predation in *E.*
767 *coli* catalase/peroxidase-deficient Hpx mutant (Δ*katA*, Δ*katG*, Δ*ahpC*). Each bar represents the
768 mean +/- SD from 3 biological replicates. Pairwise statistical comparisons were made using
769 Mann-Whitney tests, with *p*-values indicated on the graph. **(E)** Time-lapse fluorescence
770 microscopy images revealing *E. coli* intracellular ROS accumulation upon interaction with the
771 *M. xanthus* DZ2 ΔT3SS mutant, a strain that kills without lysing the prey. Before the interaction
772 with the *M. xanthus* predator, *E. coli* prey cells had been incubated with the ROS-sensitive dye
773 CM-H2DCFDA, which emits green fluorescence upon oxidation. Time points post-interaction
774 are represented at 0, 10, 20, and 30 minutes. The displayed images are representative of two
775 independent experiments. **(F)** The graph depicts mean intensity data derived from
776 approximately 700 droplets per experiment, gathered across three distinct experiments, each
777 spanning a 15-hour recording period. Within each droplet, there were approximately 20 *E. coli*
778 and 20 *M. xanthus* DZ2 cells. *E. coli* cells were pre-incubated with CM-H2DCFDA before
779 encapsulation in the droplets. Fluorescent intensity values for each condition were normalized
780 using the mean fluorescent value at the first time point to illustrate the relative increase in
781 fluorescence over time. Each data point on the graph represents the average of three
782 experiments, each encompassing around 700 droplets, with error bars indicating the standard
783 error across these three experiments.

784

Supplementary data:

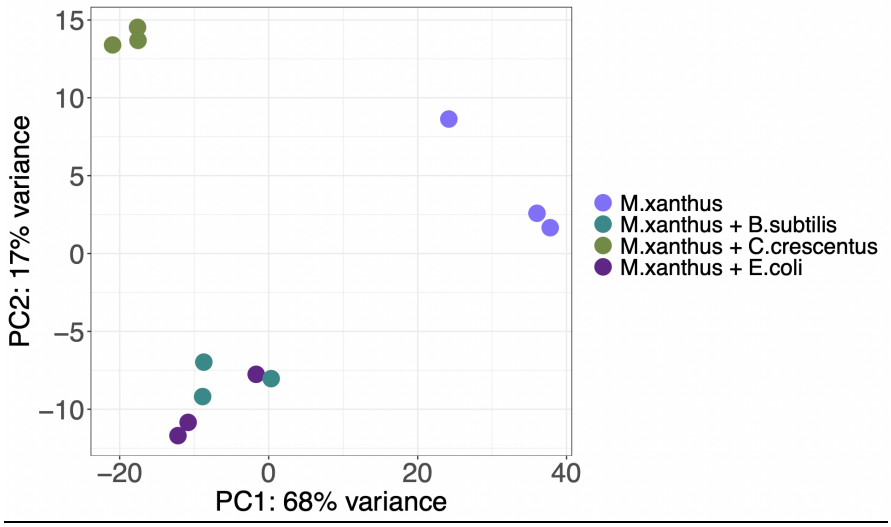

FIGURE S1: Transcriptomic response of WT to 3 different preys. Principal Component Analysis (PCA) was performed on all detected genes in RNAseq, demonstrating the consistency among replicates. Notably, the transcriptomic response to *C. crescentus* differs significantly from that of *E. coli* and *B. subtilis*, while the responses to *E. coli* and *B. subtilis* appear highly similar.

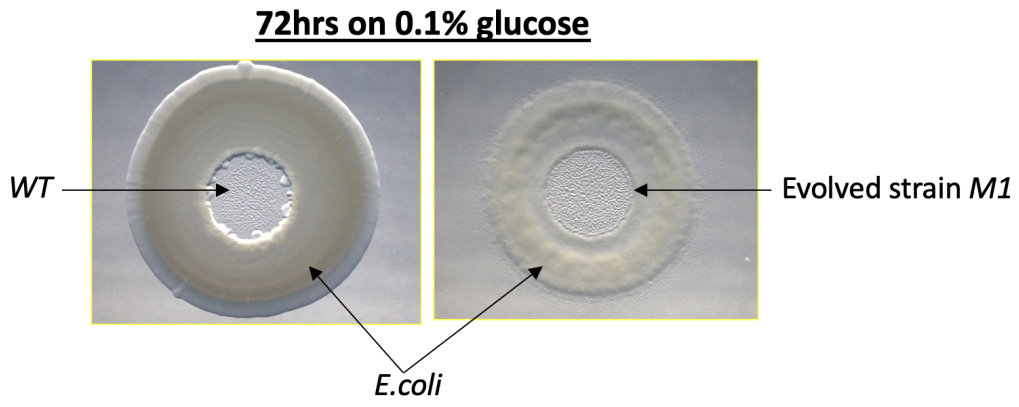

FIGURE S2: Evolved mutant M1, can kill prey on 0.1% glucose media. A 20 µL drop of *E. coli* cells, with an OD600 of 5, was deposited on 1.5% agar containing 0.1% glucose and allowed to air-dry. Subsequently, 1 µL (OD600 = 5) of *Myxococcus* cells (WT or M1) was carefully deposited at the center of the previously dried *E. coli* drop. Following a 72-hour incubation period, the M1 strain demonstrated impressive spreading capabilities, effectively colonizing and clearing the entire *E. coli* colony, whereas the WT strain failed to exhibit similar spreading behavior.

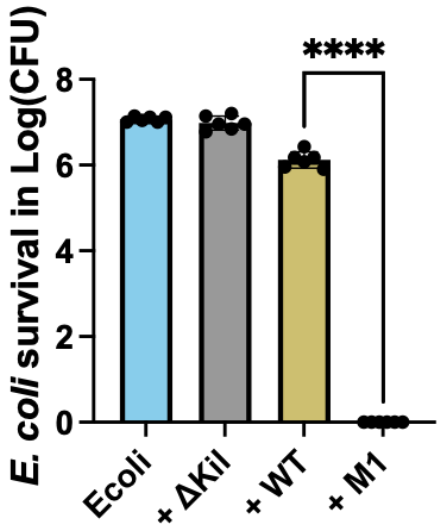

FIGURE S3: Predation efficiency of evolved mutant M1 compared to WT strain in buffered medium. The bar graph presents the average survival of *E. coli* MG1655, expressed in log10(CFU), after a 24-hour coincubation on CF media buffered at 100mM MOPS pH 7.5, with different *M. xanthus* DZ2 predators: WT, predation-deficient ΔKil, and M1 variant. Each bar represents mean +/- SD derived from 3 biological replicates. Statistical significance was determined using one-way ANOVA, with subsequent multiple comparisons conducted using the Bonferroni test; ****$p<0,0001$.

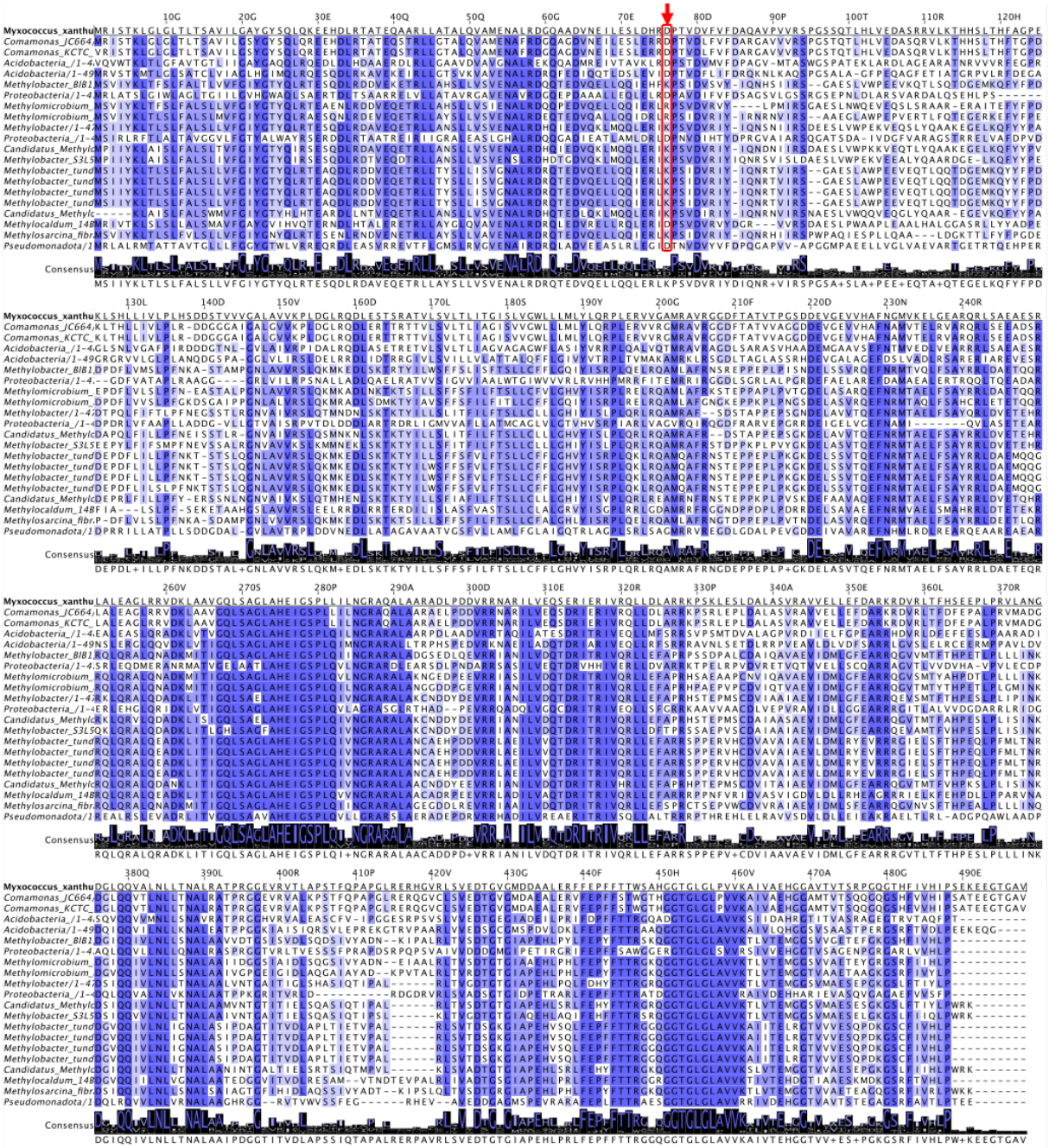

FIGURE S4: SNP in MXAN_7439 is in a non-conserved region. Protein-protein BLAST analysis was conducted using the protein sequence (WP_020478615.1) of MXAN_7439 against the NCBI non-redundant protein sequence database (nr), excluding all *Myxococcus* sequences. Hits with more than 90% query coverage and 40% sequence identity were chosen. The resulting alignment data was visualized using Jalview software(44). Sequences were color-coded based on percent identity, with the top sequence representing the reference protein (WP_020478615.1), and the others indicating homologues identified through BLAST. The position of detected SNP (D76N) in our DNA sequencing data is marked with a red arrow. The multiple sequence alignment exposes a lack of conservation in the 76th amino acid across diverse taxa, suggesting its potential non-crucial role in protein function.

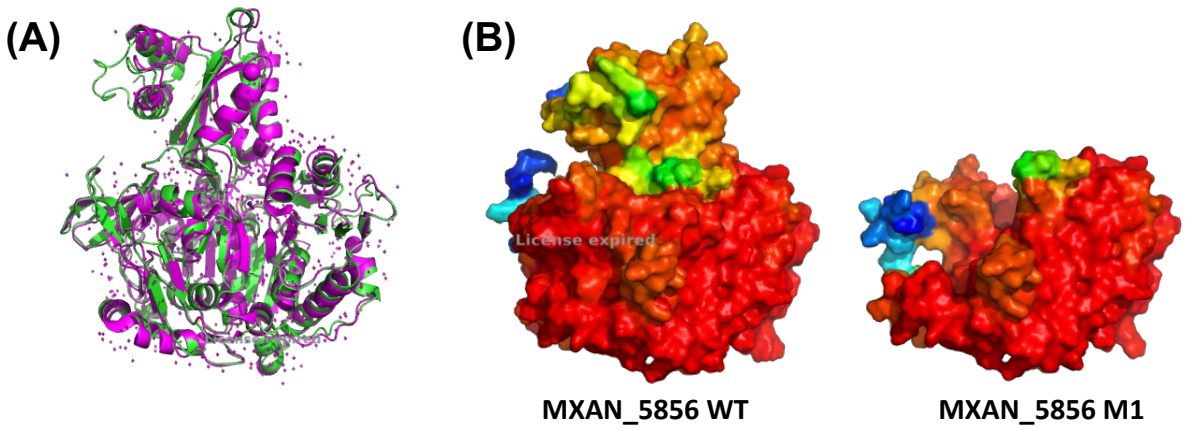

Figure S5: Structural Alignment of *M. xanthus* ACOL with *S. enterica* AcsA. (A) Superimposition of the AlphaFold2-predicted model for *M. xanthus* ACOL (MXAN_5856, green) with the experimentally resolved 3D structure of *S. enterica* AcsA (PDB: 1PG4, magenta). (B) AlphaFold2-predicted structures of the WT ACOL and the M1 mutant variant, showing the absence of the C-terminal domain in the M1 variant, which may impair enzyme activity.

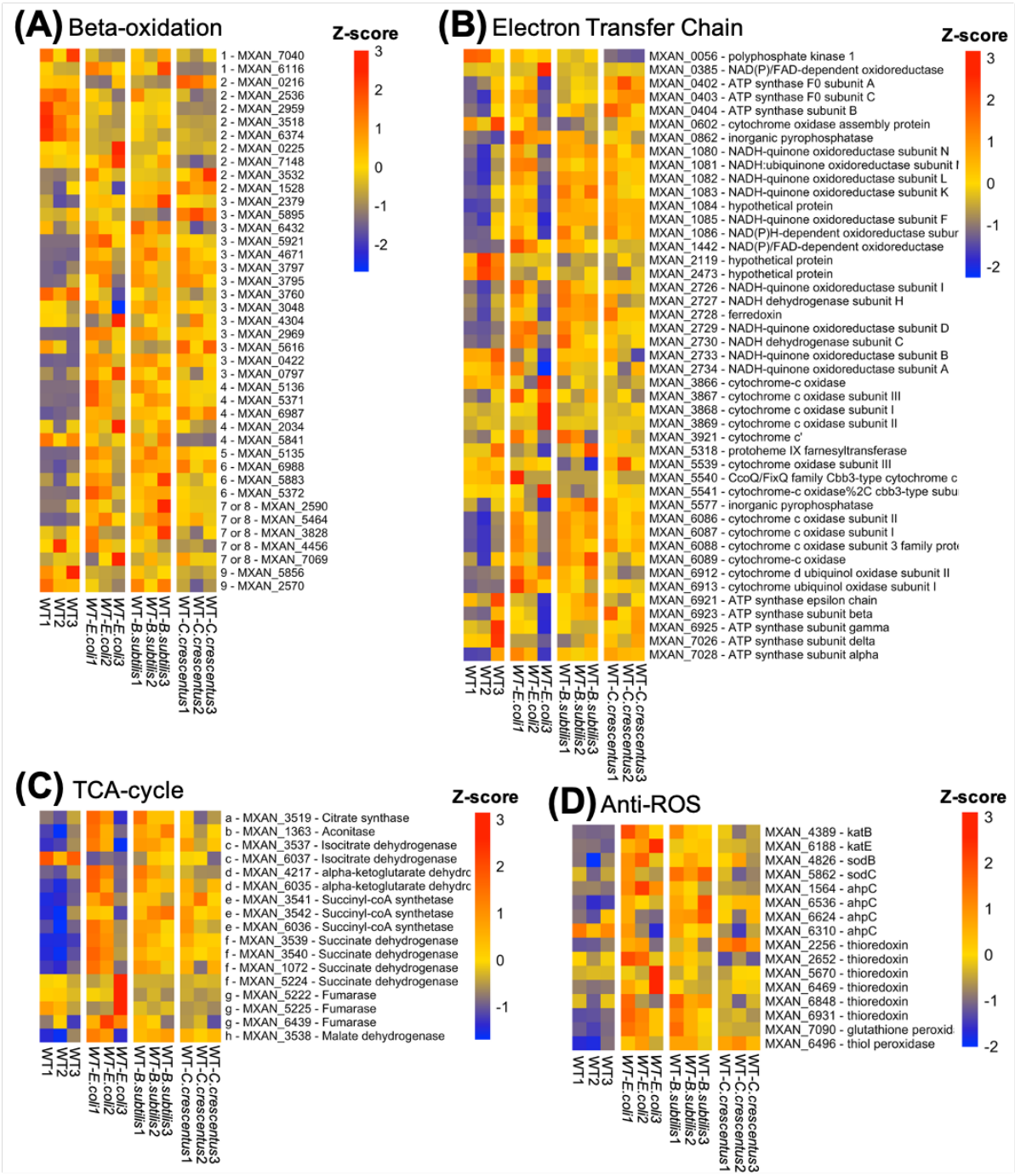

FIGURE S6: Metabolic changes during WT predation. Heatmaps display gene expression profiles, utilizing scaled DESeq2-normalized counts, with a focus on specific metabolic pathways as shown in Figure 4: **(A)** Genes related to fatty acid degradation (β-oxidation). **(B)** TCA cycle. **(C)** Electron Transfer Chain (ETC). **(D)** Antioxidant defense. Conditions compared include DZ2 WT alone, WT + *E. coli*, WT + *B. subtilis*, and WT + *C. crescentus*. Each column in the heatmaps represents an independent biological replicate.

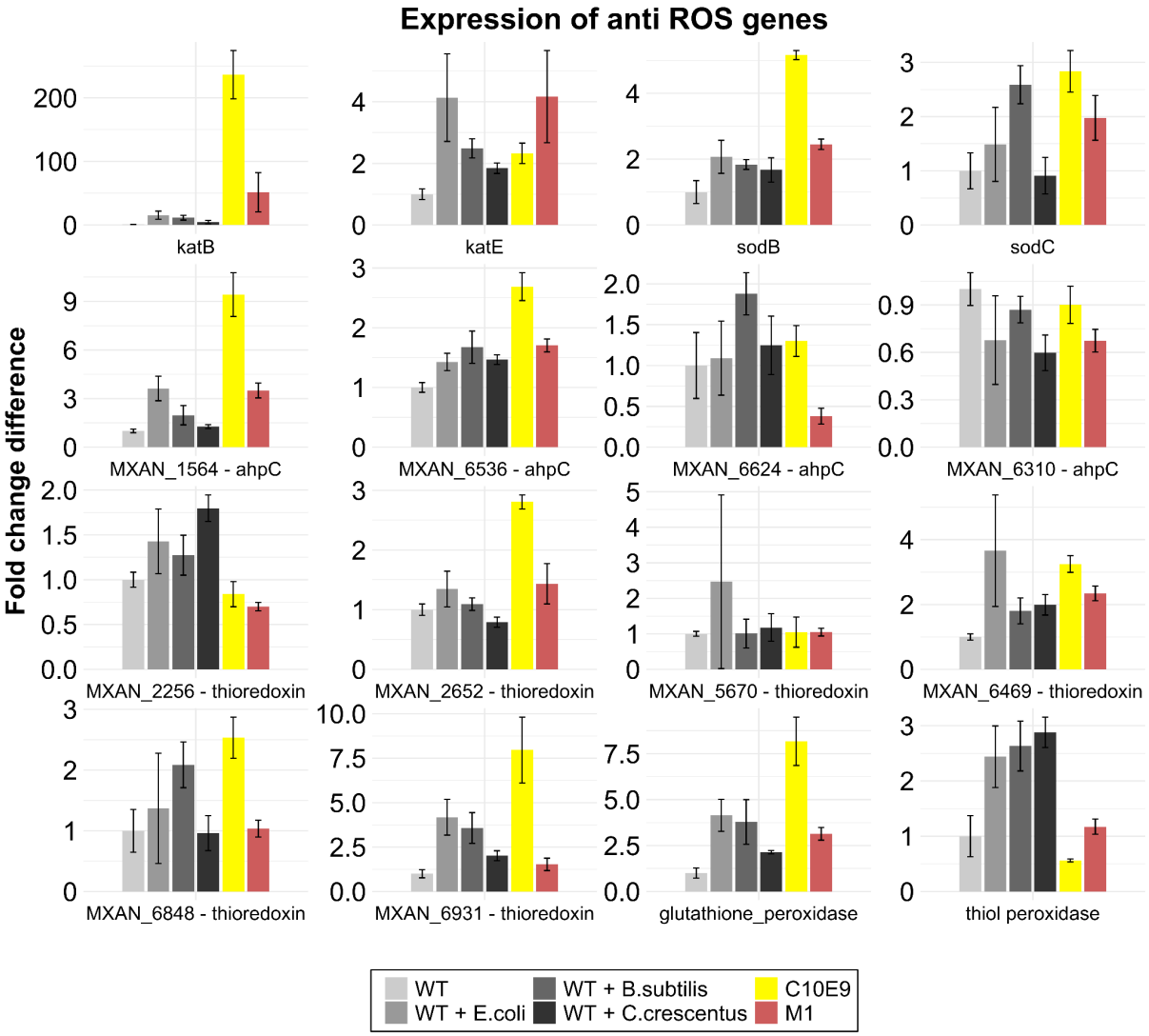

FIGURE S7: Antioxidant gene expression patterns in predation and evolved mutant variants. The bars in the graph represent the Mean ± SD of DESeq2 normalized read counts from RNAseq of 3 biological replicates. Fold Change Difference: these counts have been additionally normalized using the mean values of the Wild-Type (WT) alone condition. Conditions compared include *DZ2* WT alone, WT + *E. coli*, WT + *B. subtilis*, WT + *C. crescentus*, C10E9 alone and M1 alone.

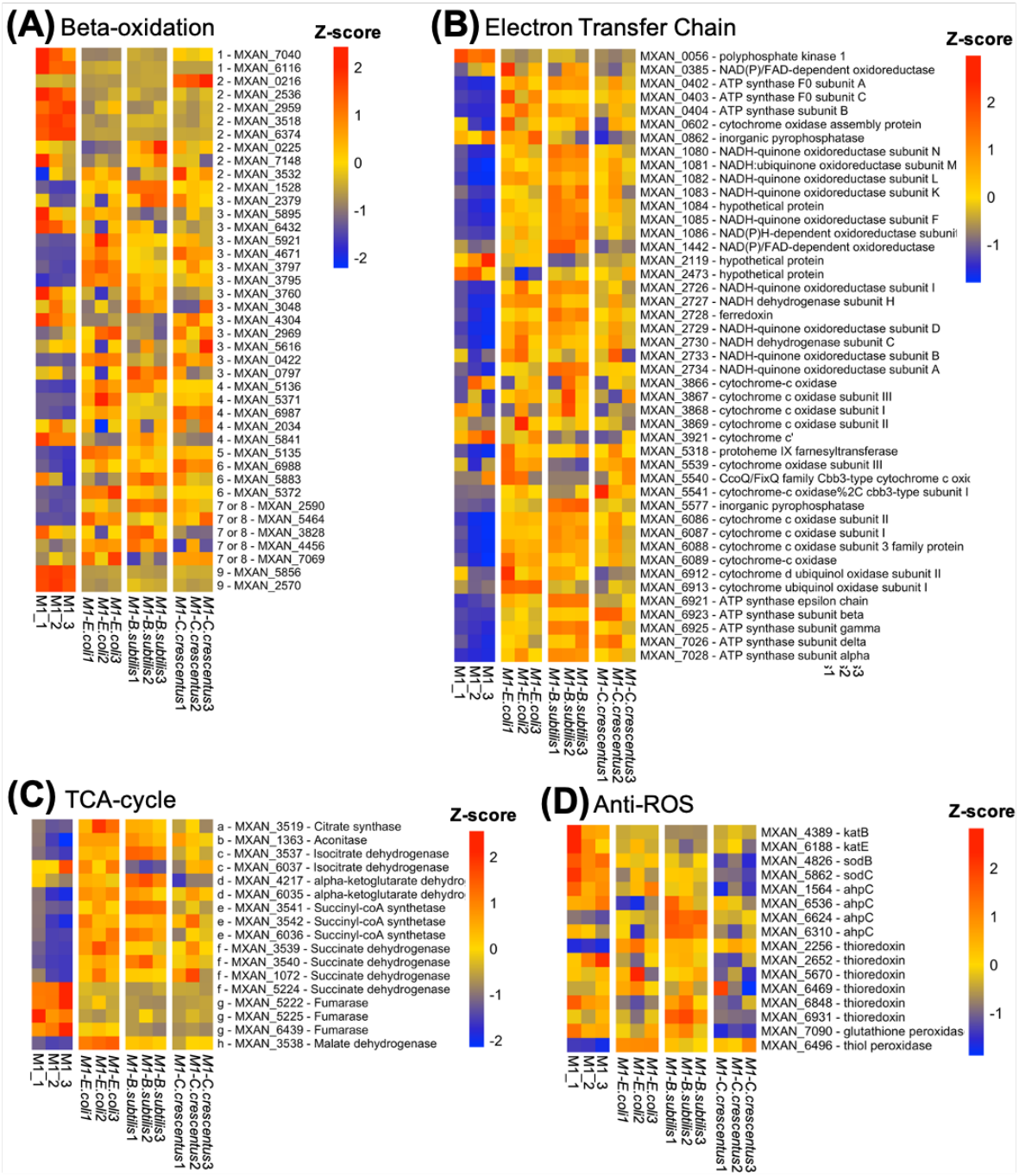

FIGURE S8: Metabolic changes during M1 predation. Heatmaps display gene expression profiles, utilizing scaled DESeq2-normalized counts, with a focus on specific metabolic pathways as shown in Figure 4: **(A)** Genes related to fatty acid degradation (β-oxidation). **(B)** TCA cycle. **(C)** Electron Transfer Chain (ETC). **(D)** Antioxidant defense. Conditions compared include M1 alone, M1 + *E. coli*, M1 + *B. subtilis*, and M1 + *C. crescentus*. Each column in the heatmaps represents an independent biological replicate.

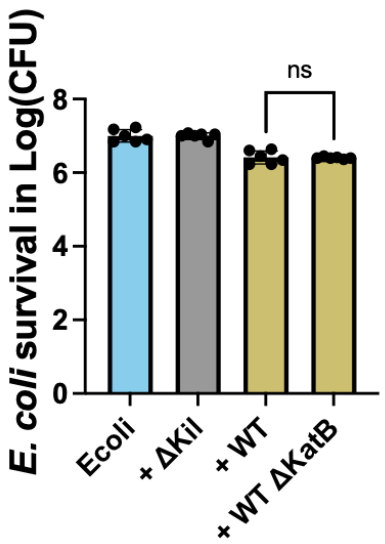

855

856 **FIGURE S9: Deletion of *katB* in DZ2 WT strain has no effect on its predation efficiency.**
857 The bar graph presents the average survival of *E. coli* MG1655, expressed in log10(CFU), after
858 a 24-hour coincubation with various *M. xanthus* DZ2 predators: WT, predation-deficient ΔKil,
859 and a *katB*-deleted variant. Each bar represents mean +/- SD derived from 3 biological
860 replicates. Statistical significance was determined using one-way ANOVA, with subsequent
861 multiple comparisons conducted using the Bonferroni test; *ns: not significant*.

862

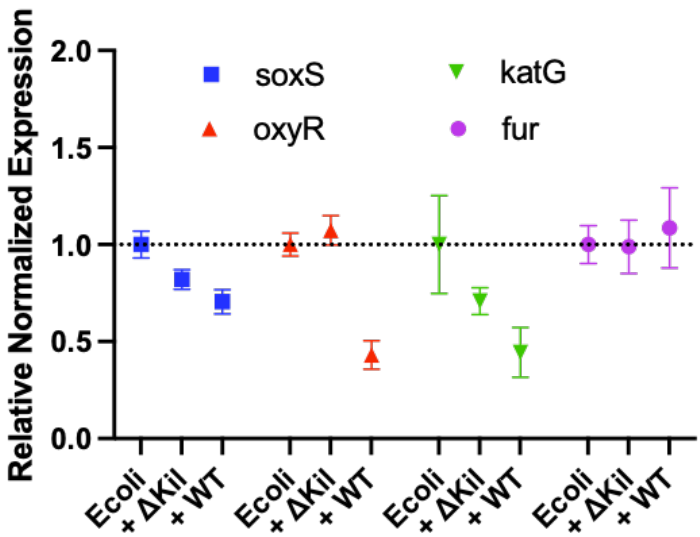

FIGURE S10: Absence of ROS-Responsive Gene Induction in *E. coli* during *M. xanthus* Predation. The expression levels of *E. coli* ROS-responsive genes (*soxS*, *oxyR*, *katG*, *fur*), following co-incubation with either *M. xanthus* DZ2 WT or its predation-deficient ΔKil mutant, were quantified via RT-qPCR. Gene expression was normalized against the housekeeping genes 16s *rrna* and *dnaK*. Data are expressed relative to the control condition (*E. coli* grown without *M. xanthus*). Mean values are plotted, and error bars indicate the standard error of the mean (SEM), derived from three independent biological replicates.

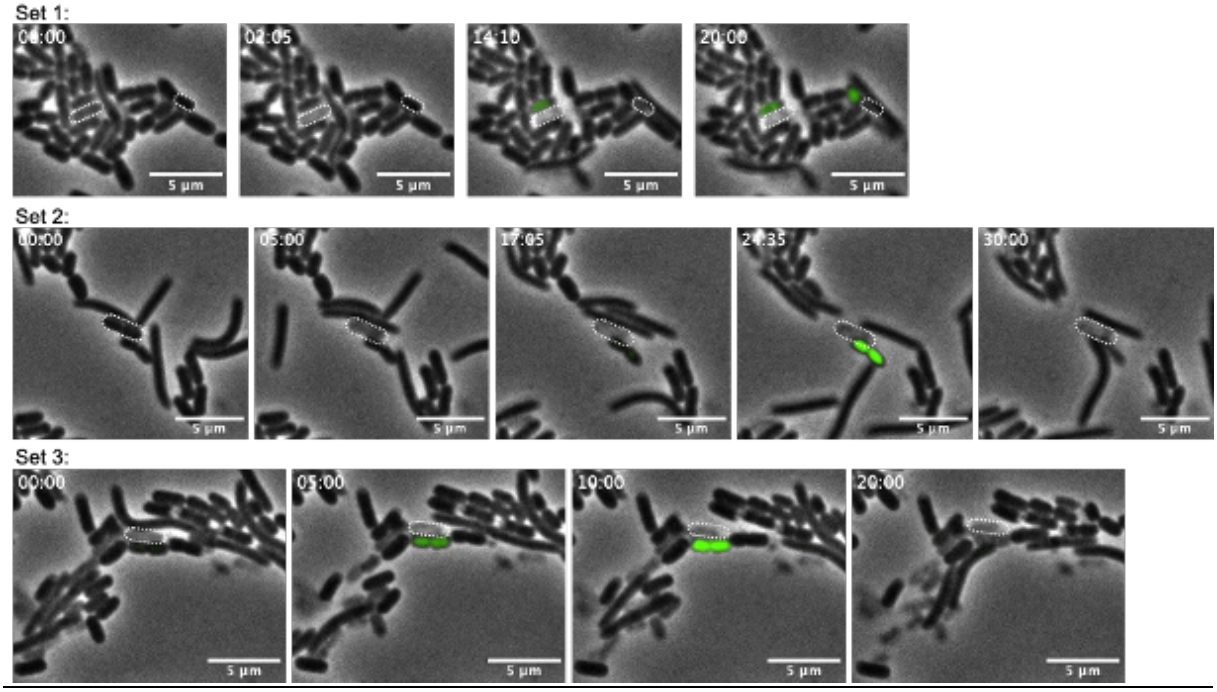

FIGURE S11: Occasional ROS Burst in Neighboring E. coli Cells Induced by Predation-Triggered Cell Lysis. Time-lapse fluorescence microscopy was used to study the interaction between *E. coli* prey cells and *M. xanthus* DZ2 WT predator cells. Prior to imaging, *E. coli* cells were stained with the ROS-sensitive dye CM-H2DCFDA. The analysis revealed that in some instances, a ROS burst was observed in *E. coli* cells adjacent to a lysed prey cell. Time points post-interaction with the predator are indicated in the images. Representative images are displayed, selected from two independent experiments.

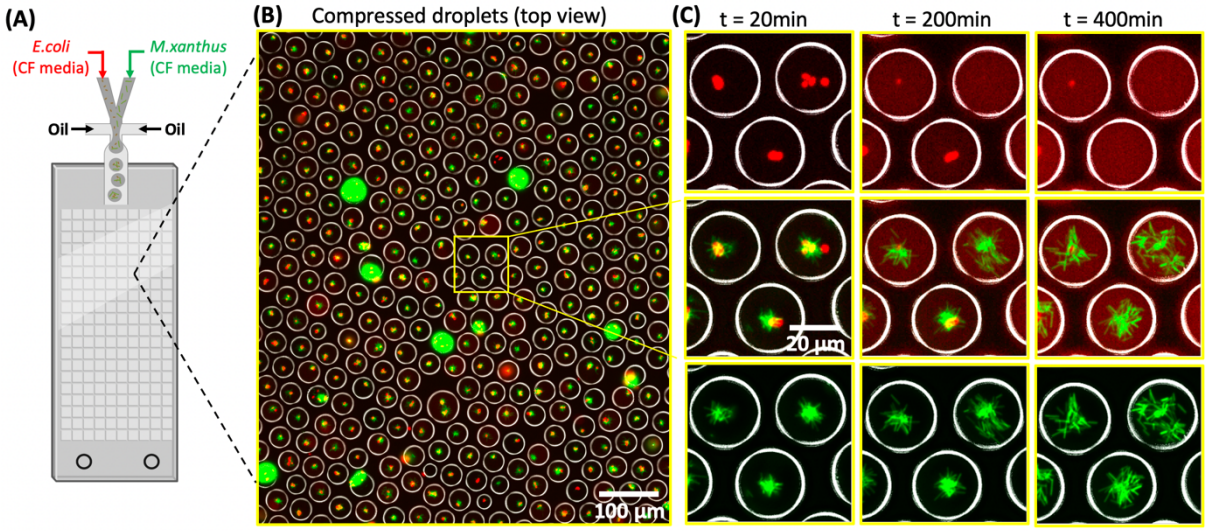

FIGURE S12: *Myxococcus* Predation inside the Microdroplets. (A) *E. coli* (OD600 = 0.7) and *M.xanthus* (OD600 = 7) suspensions, along with HFE7500 oil containing 2% FluoroSurfactant, were introduced into separate inlets of a custom droplet chip. Water-in-oil microdroplets were created using CF media, encapsulating both WT DZ-2 *Myxococcus* cells expressing GFP under *pilA* promoter and *E. coli* cells expressing mCherry in *rpsM* promoter. Droplets were pulled into a lower chamber, where they flattened into a pancake-like shape due to the reduced chamber height. **(B)** Each microdroplet contained approximately 5 *E. coli* cells and around 20 *Myxococcus* cells. **(C)** Zoomed image of select droplets extracted from panel (B) at distinct time points. In the middle row, all three channels are displayed, encompassing Bright field, Green fluorescence, and Red fluorescence. The top row shows images captured in the Bright field and Red fluorescence channels, while the bottom row showcases images acquired in the Bright field and Green fluorescence channels. Overtime fluorescent *E. coli* cells disappeared while *Myxococcus* cells multiplied showing that predation occurs within the microdroplets.

898 **SI TABLEs:**

899 Table S1: DEGs (a) alone vs *E. coli* (b) alone vs *B. subtilis* (c) alone vs *C. crescentus*
900 Table S2: 1338 common predatory genes
901 Table S3: Annotations and DESeq2 normalized count values for metabolic modules
902 Table S4: DEGs WT vs M1
903
904 Table S5: Strains
905 Table S6: Plasmids
906 Table S7: Primers
907
908 Table S8: Normalized counts - WT, WT+Ecoli, WT+Bsubtilis, WT+Ccrescentus,
909 C10E9 and M1
910 Table S9: 441 M1 DEGs similar to common predatome of WT